



Cite this: *Mater. Adv.*, 2026, 7, 942

## Low temperature green synthesis of red emitting Pb-free $\text{CsMnBr}_3$ perovskite films

Saurabh Singh, \*<sup>a</sup> Xiyu Wen<sup>b</sup> and Fuqian Yang <sup>a</sup>

Lead halide perovskites ( $\text{APbX}_3$ ) have demonstrated exceptional opto-electronic properties, but their inherent toxicity and environmental hazards hindered their practical deployment in display technologies such as liquid crystal display (LCD) backlights. Herein, we report for the first time a facile, water-mediated synthesis of red-emitting  $\text{CsMnBr}_3$  thin films from an aqueous solution of  $\text{CsBr}$  and  $\text{MnBr}_2$  precursors at a low temperature of  $\sim 50$  °C. Unlike traditional synthesis routes reported for synthesis of  $\text{CsMnBr}_3$  powders or nanocrystals, relying heavily on toxic solvents, high temperatures, or inert atmospheres, the green approach utilizes water as a benign medium to facilitate the  $[\text{MnBr}_6]$  octahedral coordination assembly, yielding continuous red films with strong photoluminescence ( $\lambda$ :  $\sim 644$  nm, FWHM:  $\sim 75$  nm). The as-synthesized  $\text{CsMnBr}_3$  films exhibit remarkable optical quality with an ultra-wide color gamut coverage ( $\sim 132\%$  of NTSC 1953 and  $\sim 186\%$  of sRGB color standards), making them a promising alternative for traditional red phosphors in LCD backlight applications. The characterization of electrical and photo-responses reveals a negative photoconductivity under UV irradiation, attributed to the powdered microstructure and hygroscopic nature of  $\text{MnBr}_2$  under ambient air conditions. The photo-response of the red-emissive  $\text{CsMnBr}_3$  films exhibits a power-law dependence on high-energy irradiation under ambient conditions at  $\sim 18$  °C and a relative humidity of  $\sim 65\%$ , along with faster self-recovery behavior, highlighting the complex role of defect-mediated charge transport. This green, low-cost, and scalable synthesis route offers a promising pathway toward sustainable and lead-free phosphor materials for next-generation wide-color-gamut display technologies.

Received 30th October 2025,  
Accepted 23rd November 2025

DOI: 10.1039/d5ma01256b

[rsc.li/materials-advances](http://rsc.li/materials-advances)

## 1. Introduction

Metal halide perovskites have shown great promise over the past decade to revolutionize next-generation energy and opto-electronic devices such as light-emitting diodes (LEDs), and display technologies, due to their tunable band gaps, high defect tolerance, high thermal resilience, strong light absorption, high photoluminescence quantum yields (PLQY), and facile solution processability.<sup>1–3</sup> Among a wide family of perovskites, all-inorganic halide perovskite systems (such as  $\text{CsBX}_3$ , B = Pb, Sn, Mn, and X = Cl, Br, I) overpower hybrid organic–inorganic systems owing to their superior thermal and environmental stability while maintaining their excellent opto-electronic properties including higher color purity and higher defect tolerance, making them particularly attractive for device integration and optimization.<sup>4,5</sup>

There are serious concerns, such as lead toxicity and their long-term environmental hazards, which have hindered further

growth and inclusivity of lead-based halide perovskites ( $\text{APbX}_3$ ) in high-performance photovoltaic and display technologies. Also, common synthesis approaches for producing lead halide perovskites ( $\text{APbX}_3$ ), such as hot injection,<sup>6</sup> LARP,<sup>7</sup> ultrasonic,<sup>8</sup> solvothermal<sup>9</sup> and microwave assisted,<sup>10</sup> further pose greater challenges, hindering their large-scale commercialization, due to the involvement of high temperature, high vacuum and inert environments, high cost, toxic polar and non-polar solvents of DMF, DMSO, hexane and toluene, low reproducibility, excessive external energies, and complex synthesis processes.<sup>9,11–13</sup> Therefore, the need to explore alternative cations such as Sn, Mn, Bi, Sb, and double perovskites, and develop eco-friendly processes has become imperative, although their stability and toxicity trade-offs remain significant.<sup>14</sup>

Manganese-based halide perovskites (e.g.,  $\text{CsMnCl}_3$  and  $\text{CsMnBr}_3$ ) have attracted a significant amount of attention, given that  $\text{Mn}^{2+}$  is relatively less toxic than  $\text{Pb}^{2+}$  cations and exhibits a bright and efficient photoluminescence (PL) red emission arising from the spin- and parity-forbidden d–d ( $^4\text{T}_1$  to  $^6\text{A}_1$ ) transitions within the  $[\text{MnBr}_6]$  octahedra of the  $\text{CsMnBr}_3$  lattice.<sup>15–17</sup> This red PL emission is particularly valuable for display technologies, where deep-red emitters are required for wide gamut color reproduction for backlight

<sup>a</sup> Materials Program, Department of Chemical and Materials Engineering, University of Kentucky, Lexington, KY 40506, USA. E-mail: ssi303@uky.edu

<sup>b</sup> Center for Aluminium Technology, University of Kentucky, Lexington, KY 40506, USA



units (BLUs) in liquid crystal displays (LCDs).<sup>18</sup> However, conventional red phosphors such as rare-earth nitride phosphors, Mn<sup>4+</sup> fluorides, and cadmium quantum dots, often suffer from high synthesis costs,<sup>19</sup> limited tunability,<sup>20</sup> synthesis complexity,<sup>19</sup> environmental impact,<sup>21</sup> low color purity,<sup>20</sup> and poor thermal or moisture stability,<sup>22</sup> whereas Mn-based perovskites such as CsMnBr<sub>3</sub> offer low-cost, lead-free, and tunable alternatives for these traditional phosphor materials.<sup>15,23,24</sup>

Despite these lucrative advantages, synthesizing high-quality red-emitting CsMnBr<sub>3</sub> films remains challenging to date as most synthesis methods typically involve solid-state synthesis, microwave-assisted synthesis, or colloidal hot-injection routes, which predominantly yield red-emitting powders or nanocrystals rather than continuous red-emitting thin films suitable for device integration.<sup>17,25–27</sup> Moreover, these approaches typically involve toxic solvents, surfactants, elevated temperatures, and inert environments, which limit the scalability and compatibility with low-cost device fabrication.<sup>17,25–27</sup> For instance, Almutlaq *et al.*<sup>15</sup> reported a hot-injection method to produce red-emitting CsMnBr<sub>3</sub> nanocrystals, requiring high temperature ( $\sim 170$  °C), an inert environment, and toxic solvents such as octadecene (ODE) and hexane, thereby raising significant environmental concerns. Interestingly, Sahu *et al.*<sup>27</sup> employed a microwave-assisted approach to synthesize red-emitting CsMnBr<sub>3</sub> crystals. However, this approach is limited by demands of high vacuum and inert environments for the preparation of a Cs-oleate precursor, complicated synthesis conditions, and a non-stoichiometric excess of MnBr<sub>2</sub> (an optimized molar ratio of Cs<sub>2</sub>CO<sub>3</sub>:MnBr<sub>2</sub> was 1:7). Gao *et al.*<sup>16</sup> reported a solid-state synthesis of CsMnBr<sub>3</sub> powders exhibiting bright red emission at  $\sim 650$  nm, but is challenged by non-uniform film formation and poor substrate adhesion issues.

Recent advances in halide-based luminescent materials further highlight the importance of film or composite morphologies for functional opto-electronic applications.<sup>28,29</sup> For instance, Cai *et al.*<sup>29</sup> demonstrated the potential of CsPbBr<sub>3</sub>/PS composites for ultrawide-range wearable temperature sensors, while Cai *et al.*<sup>28</sup> incorporated CsPbBr<sub>3</sub>/PDMS nanospheres for multi-dimensional sensing and interactive displays. However, continuous emissive films of pure CsMnBr<sub>3</sub> remain unexplored, leaving a clear gap for device-compatible, red-emitting lead-free halide films. Therefore, fabricating a continuous, red emissive CsMnBr<sub>3</sub> films is crucial as unlike powders or nanocrystals, continuous CsMnBr<sub>3</sub> films would allow direct device integration, ensure uniform optical properties, and enable charge transport and photoconductivity characterization, which are inaccessible in non-film morphologies. Additionally, solution-processable film deposition approaches can improve scalability, reduce reliance on toxic solvents, and expand compatibility with standard thin-film optoelectronic fabrication techniques.<sup>30</sup>

In this work, we report for the first time a simple, low-cost, and facile green synthesis of red-emitting CsMnBr<sub>3</sub> thin films at a low temperature of  $\sim 50$  °C *via* thermal evaporation of an aqueous solution containing CsBr and MnBr<sub>2</sub> precursors in a molar ratio of 1:2. Unlike conventional toxic solvents (*e.g.*, ODE, hexane, and DMF/DMSO), water acts as green and

low-cost medium enhancing ionic transport and facilitating the assembly of [MnBr<sub>6</sub>] octahedral coordination, yielding red-emissive CsMnBr<sub>3</sub> films ( $\lambda$ :  $\sim 644$  nm, FWHM:  $\sim 75$  nm) directly in aqueous solutions. The as-synthesized CsMnBr<sub>3</sub> films exhibited an ultra-wide gamut coverage area of  $\sim 132\%$  of NTSC 1953 and  $\sim 186\%$  of sRGB color standards, thereby demonstrating their strong potential as an alternative to conventional red phosphors used in wide color gamut display applications (such as LCD backlights). This simple water-mediated synthesis route to produce red-emissive CsMnBr<sub>3</sub> films opens up new avenues for scalable, low-toxicity, easily processable, reproducible, and device-compatible phosphor materials, addressing both the sustainability and performance needs of next-generation display technologies.

## 2. Experimental details

### 2.1. Synthesis of CsMnBr<sub>3</sub> films

CsBr (99.9%, Beantown Chemical) and MnBr<sub>2</sub> ( $\geq 97\%$ , Strem Chemicals Inc.) powders were mixed in a 1:2 molar ratio in 2 mL of DI water to obtain a precursor solution. 100  $\mu$ L of this precursor solution was drop-casted on a cleaned Cu substrate, which was vacuum-dried at  $\sim 50$  °C to obtain crystallized films, as shown in Fig. 1, for further characterization.

### 2.2. Synthesis of CsPbBr<sub>3</sub>-PMMA films for LCD backlights

CsPbBr<sub>3</sub> films used as green convertor film in white LCD backlights were prepared *via* the standard LARP method, where CsBr (0.4 mmol) (99.9%, Beantown Chemical) and PbBr<sub>2</sub> (0.4 mmol) ( $> 98\%$ , Strem Chemicals Inc.) were mixed in 10 mL of DMF (VWR) with 1 mL of oleic acid (Ward's Science) and 0.5 mL of oleylamine ( $> 50\%$ , TCI America). The resulting mixture was stirred at 20 °C overnight to form a precursor solution. 1 mL of this prepared precursor solution was quickly dripped in 10 mL of toluene (VWR) under vigorous stirring at 20 °C to form CsPbBr<sub>3</sub> nanocrystals. The precursor solution was added to a PMMA solution (formed *via* dissolving PMMA powders ( $M_w = 35\,000$ ) (Fisher Scientific) in toluene in 0.02 g mL<sup>-1</sup> concentration). The formed PMMA solution was coated on glass slides of  $0.80 \times 6.66 \times 72.62$  mm<sup>3</sup> in dimensions, ultimately forming CsPbBr<sub>3</sub>-PMMA films.

### 2.3. Materials characterization

The morphological and chemical compositional analyses were conducted on a scanning electron microscope (SEM) (JEOL JSM-5900LV) equipped with an energy-dispersive X-ray spectrometer (EDS). The structural characterization of the as-prepared CsMnBr<sub>3</sub> films was performed on an X-ray diffractometer (XRD) (Siemens D500) with CuK $\alpha$  radiation ( $\lambda = 1.5406$  Å). X-ray photoelectron spectroscopy (XPS) (Thermo Scientific K-alpha X-ray photoelectron spectrometer) was utilized to analyze the chemical composition of the as-prepared CsMnBr<sub>3</sub> films. The Photoluminescence studies of the as-prepared CsMnBr<sub>3</sub> films were carried out using a spectrometer (Ocean optics, FLAME-S-VIS-NIR-ES, Ocean Optics) under a UV excitation wavelength of



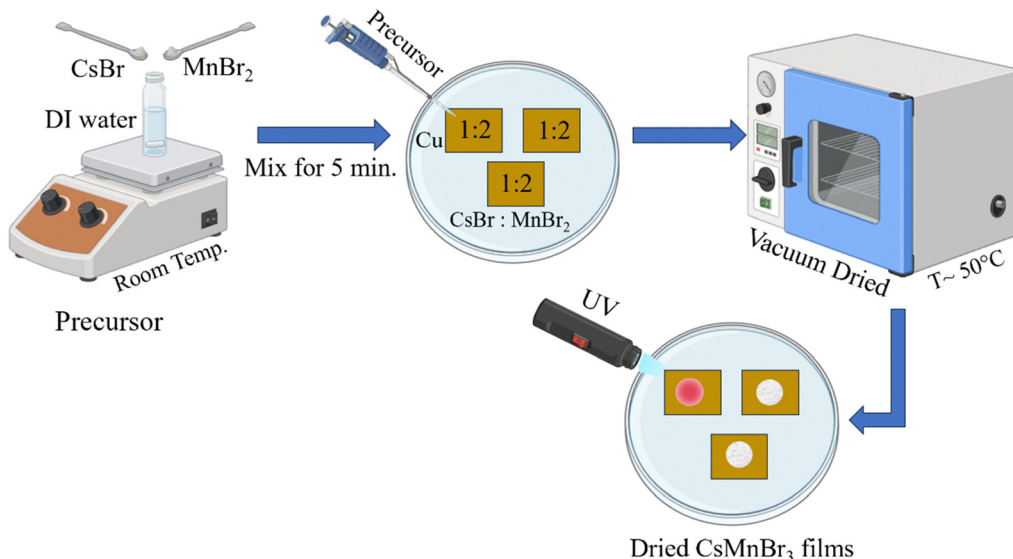


Fig. 1 Schematic depicting the synthesis route of  $\text{CsMnBr}_3$  films via an aqueous solution of  $\text{CsBr}$  and  $\text{MnBr}_2$  in a 1:2 molar ratio.

365 nm. Absolute photoluminescence quantum yield (PLQY) measurements of  $\text{CsMnBr}_3$  films were conducted on a Horiba Scientific Fluoromax Plus-C fluorometer in which a solid sample was mounted on a sample stage and placed in an integrating sphere. An excitation wavelength of 365 nm was used for PLQY measurements with a 1 nm slit width and a 0.1 s integration time. The Raleigh scattering peak of the excitation and the PL from these  $\text{CsMnBr}_3$  films were extracted *via* scanning the emission in a range of 345–710 nm. A blank copper substrate without specimen was also scanned in the same scanning range of 345–710 nm for reference. Furthermore, PLQY calculations were performed using Horiba Scientific FluorEssence™ software with a factory acquired integrating sphere correction defined as  $\text{PLQY} = ((\text{PB} - \text{PA}) / (\text{LA} - \text{LB})) \times 100\%$ , where  $(\text{PB} - \text{PA})$  is the number of emitted photons,  $(\text{LA} - \text{LB})$  is the number of absorbed photons, respectively. The lifetime decay studies were conducted using a DeltaHub™ high throughput time correlated single photon counting (TCSPC) controller. The electrical responses ( $I$ - $V$ ) of the as-prepared  $\text{CsMnBr}_3$  films were investigated using a Keithley 2400 source-meter (Keithley, Solon, OH, USA) under white and UV irradiation.

### 3. Results

Fig. 2a–c depicts schematically the crystal structure of  $\text{CsMnBr}_3$  along the  $a$ ,  $b$ , and  $c$  crystallographic axes, respectively, highlighting strongly coupled one-dimensional connectivity of the  $[\text{MnBr}_6]$  octahedra for red photoluminescence of the material.<sup>15,17,26,31</sup> Fig. 2d presents the surface morphology (SEM micrograph) of the as-prepared  $\text{CsMnBr}_3$  films with a densely packed granular structure, suggesting successful formation of  $\text{CsMnBr}_3$  microcrystals at  $\sim 50$  °C. The microcrystals are irregularly shaped but interconnected, which is favorable for charge transport in optoelectronic applications.

The analysis of the size distribution (Fig. 2e) demonstrates a near-normal distribution with a mean size of  $0.62 \pm 0.17$   $\mu\text{m}$ . The EDS analysis, as shown in Fig. S1 (SI), confirms a 1:1:3 atomic ratio of Cs:Mn:Br in the as-prepared films, consistent with the stoichiometric  $\text{CsMnBr}_3$ .

The XRD pattern of the as-deposited  $\text{CsMnBr}_3$  films is presented in Fig. 2f. A set of diffraction peaks are observed around  $\sim 26.58^\circ$ ,  $29.95^\circ$ ,  $43.1^\circ$  and  $43.36^\circ$ , corresponding to the (200), (201), (301), and (103) planes of the hexagonal phase of  $\text{CsMnBr}_3$  with a space group of  $P6_3/mmc$  (PDF #97-000-9703). Using Bragg's law (eqn (S1)<sup>32</sup> in the SI) and the hexagonal system's  $d$ -spacing equation (eqn (S2)<sup>33</sup> in the SI), the lattice constants are calculated to be  $a \sim 7.63$   $\text{\AA}$  and  $c \sim 6.97$   $\text{\AA}$ , which are in good accordance with the reported results on the  $\text{CsMnBr}_3$  structure.<sup>16,31</sup> However, all the observed Bragg peaks exhibit a left shift toward lower diffraction angles compared to the standard pattern, indicating lattice expansion as explained by Bragg's Law<sup>32</sup> (eqn (S1)). Such shifts are well reported for perovskite materials.<sup>34–39</sup> The leftward shift with some peak broadening likely can be attributed to transient hydration or intercalation of water during crystallization<sup>37,40</sup> and defect-induced micro-strain. Note that moderate secondary peaks related to  $\text{CuBr}_2$  ( $\sim 17$  wt%) and  $\text{MnO}_2$  ( $\sim 10$  wt%) were also detected (Fig. 2f) in addition to the dominant phase  $\text{CsMnBr}_3$  ( $\sim 73$  wt%), likely arising from the residues of precursors. These values were estimated from the relative intensities of representative phase reflections, likely representing an upper bound for impurity contents. Although, these impurity phases may introduce localized non-radiative trap states or scattering centers at grain boundaries, potentially reducing photoluminescence quantum yield or charge-carrier mobility,<sup>41–43</sup> a relatively moderate fraction of such impurities suggests that the film's opto-electronic performance is likely governed by the dominant red-emissive  $\text{CsMnBr}_3$  phase, with only slight quenching from these impurity phases, respectively.



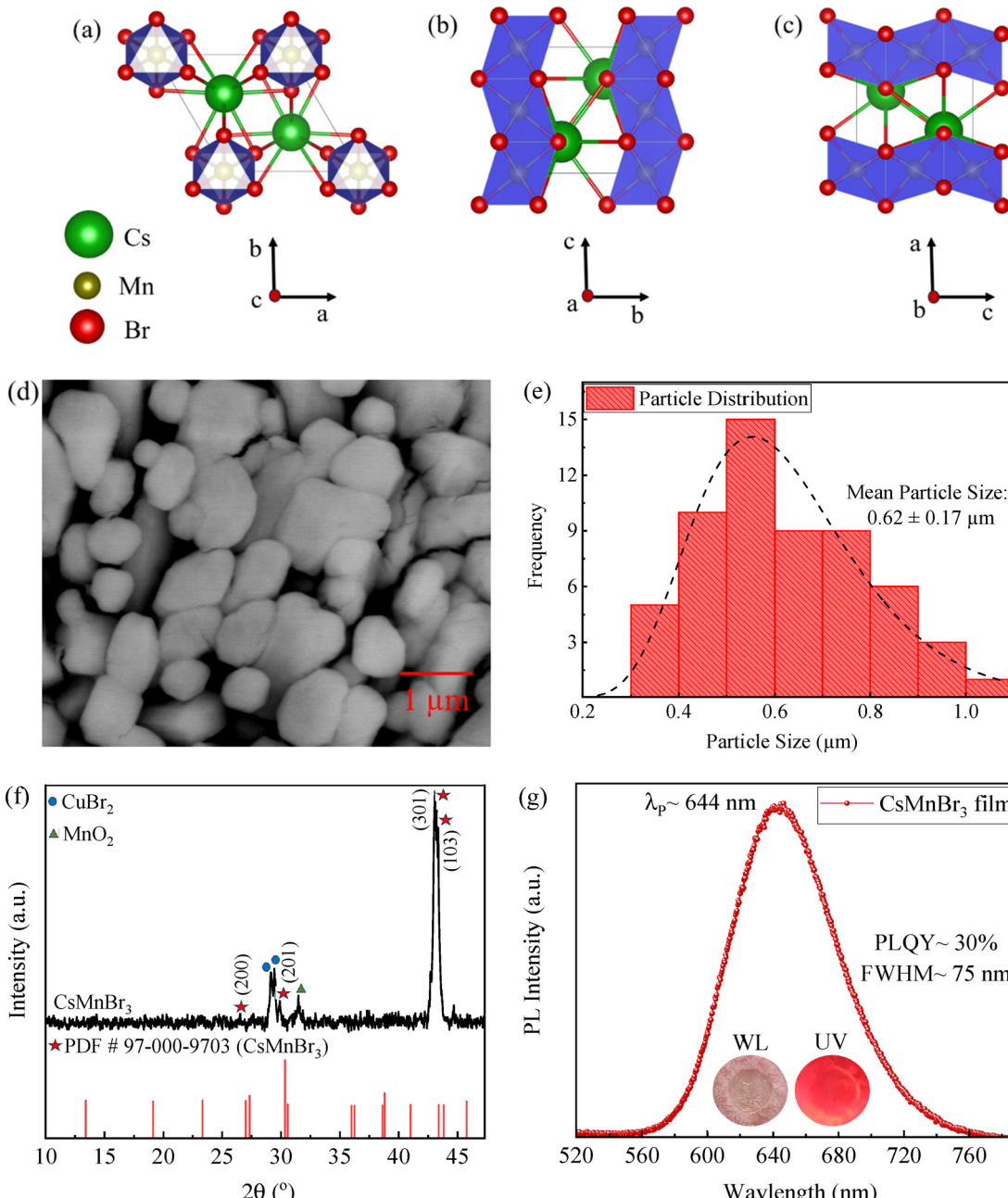


Fig. 2 Crystal structure of  $\text{CsMnBr}_3$  projected along (a)  $c$ -axis, (b)  $a$ -axis, and (c)  $b$ -axis, (d) a SEM image of the as-prepared  $\text{CsMnBr}_3$  film, (e) histograms depicting the distribution of particle sizes, (f) XRD spectra of the as-prepared  $\text{CsMnBr}_3$  film, and (g) PL spectra of the as-prepared  $\text{CsMnBr}_3$  film with the inset showing optical images of the film under white and UV light ( $\sim 365 \text{ nm}$ ), respectively.

Fig. 2g shows the PL spectrum of the  $\text{CsMnBr}_3$  film deposited on a Cu substrate under UV excitation of  $\sim 365 \text{ nm}$ , depicting a broad peak (FWHM  $\sim 75 \text{ nm}$ ) centered at  $\sim 644 \text{ nm}$  and exhibiting photoluminescence quantum yield (PLQY) of  $\sim 30\%$ , respectively. This emission arises from the characteristic d-d transitions of octahedrally coordinated  $\text{Mn}^{2+}$  ions, successfully excited under a high-energy UV source ( $\lambda \sim 365 \text{ nm}$ ) and is consistent with the reports in the literature.<sup>15,44,45</sup> For instance, Almutlaq *et al.*<sup>15</sup> reported a broad PL spectrum (FWHM:  $\sim 78 \text{ nm}$ ) for colloidal  $\text{CsMnBr}_3$  centered at  $\sim 643 \text{ nm}$  arising due to d-d transitions

of  $\text{Mn}^{2+}$  ions in octahedral coordination from a low energy excited state ( ${}^4\text{T}_1$ ) to the corresponding ground state ( ${}^6\text{A}_1$ ). The insets in Fig. 2g display the optical images of the as-prepared  $\text{CsMnBr}_3$  films, exhibiting bright red emission under UV irradiation ( $\lambda: \sim 365 \text{ nm}$ ) and validating the effectiveness of the high energy UV light in exciting the  $\text{Mn}^{2+}$  transitions responsible for red emission.<sup>46,47</sup> Furthermore, the Cu substrate was explicitly chosen for deposition of  $\text{CsMnBr}_3$  films owing to its high electrical conductivity and compatibility with our experimental setup. Although copper is known to be chemically active and may tend

to react with halide species to form copper halides or other by-products,<sup>48,49</sup> several factors might limit such interactions under our synthesis conditions namely rapid solvent (water) evaporation during deposition, brief halide–substrate contact, and the absence of any acidic or strongly oxidative species to promote Cu halide formation. Moreover, X-ray diffraction spectra (Fig. 2f) also revealed minor peaks corresponding to CuBr<sub>2</sub> and MnO<sub>2</sub>, indicating trace impurity formation, while preserving the dominant red emitting CsMnBr<sub>3</sub> phase. Importantly, photoluminescence measurements conducted on both copper (Cu) and glass substrates (Fig. S3) exhibited similar PL emission spectra, confirming that the observed optical properties (Fig. 2g) are intrinsic to the CsMnBr<sub>3</sub> phase and are not significantly affected by the utilization of the Cu substrate.

Thereafter, the as-prepared CsMnBr<sub>3</sub> films were also exposed to blue LED light of ~450 nm in wavelength. The PL spectrum is presented in Fig. 3a together with the one under UV light of ~365 nm in wavelength. The films exhibit the nearly same red PL emission with a peak centered around ~644 nm, supporting that the observed characteristic luminescence originates from the intrinsic d-d transition of Mn<sup>2+</sup> ions, *i.e.*, the spin- and parity-forbidden transitions [excited 4T<sup>1</sup> state to ground 6A<sup>1</sup> state] within the octahedral [MnBr<sub>6</sub>] coordination environment.<sup>15,26,50,51</sup> The nearly same red emission under different excitation wavelengths highlights the robust optical response of the as-prepared CsMnBr<sub>3</sub> films *via* the green route and further validates their suitability as stable red emitters in optoelectronic applications.

The photo-emission characteristics of CsMnBr<sub>3</sub> films were evaluated using the CIE chromaticity diagram (Fig. 3b). The CsMnBr<sub>3</sub> films exhibit CIE color coordinates of (~0.60, ~0.30), placing them within the red region of the standard CIE 1931 color space. This is well in accord with the PL emission peak at ~644 nm. Such chromaticity positions are highly desirable for opto-electronic applications as they align closely with the red color gamut requirements of different standard color spaces such as NTSC and sRGB.<sup>52–55</sup>

The long-term stability of CsMnBr<sub>3</sub> films was examined under both vacuum and ambient conditions (*T*: ~17 °C, relative humidity (RH): ~65%), as shown in Fig. 3c–h, respectively. Fig. 3c depicts the time-dependent PL spectra of the CsMnBr<sub>3</sub> films in a vacuum environment, monitored over a period of 12 days. A gradual decrease in PL intensity with a small blue shift in PL wavelength was observed with respect to increasing time. This is in contrast to the PL spectra observed for the CsMnBr<sub>3</sub> films under ambient conditions (*T*: ~17 °C, RH: ~65%), as shown in Fig. 3d, which experienced a faster degradation in PL intensity and a significant blue shift of PL wavelength and limited stability to several hours in ambient environments.

The time dependent PL intensities and PL wavelengths are extracted from Fig. 3c and d and plotted independently for both the vacuum and ambient conditions, as shown in Fig. 3e–h. The PL intensity of CsMnBr<sub>3</sub> films exhibits slower decay under the vacuum conditions (Fig. 3e) in contrast to rapid decay under ambient conditions, as shown in Fig. 3f, respectively.

Both the decay behavior follows exponential dependence on time, as illustrated by the fitting curves. The enhanced PL stability of the as-prepared CsMnBr<sub>3</sub> films in the vacuum environment might be attributed to the absence of extrinsic degradation pathways, such as oxygen and moisture-induced halide oxidation, and/or hydrolysis reactions, which generally accelerate the non-radiative recombination processes for faster PL quenching over time.<sup>56–61</sup>

The peak emission wavelength of CsMnBr<sub>3</sub> films experiences a small linear blue shift from ~644 nm to ~641 nm within 12 days under the vacuum conditions (Fig. 3g), in contrast to a rapid exponential blue shift under ambient conditions (*T*: ~17 °C, RH: ~65%) from ~644 nm to ~612 nm within 3 hours, as shown in Fig. 3h. This further highlights the slower structural and/or surface-related relaxation processes, such as minor lattice contraction and/or defect reconfiguration, experienced by the as-synthesized CsMnBr<sub>3</sub> films in the vacuum environment.<sup>56–61</sup>

The observed unstable PL characteristics of CsMnBr<sub>3</sub> films under ambient conditions (Fig. 3f and h) can be attributed to an array of factors such as moisture-induced halide migration and structural lattice distortions<sup>56–61</sup> and inherent hygroscopic and deliquescent nature of MnBr<sub>2</sub> (utilized in the precursor formation), which is highly soluble in water<sup>62–65</sup> and hence readily absorbs atmospheric moisture, especially in low temperature and high humid environments. This accelerates the hydrolysis process of Mn–Br bonds and ultimately destabilizes the [MnBr<sub>6</sub>] octahedra present inside the CsMnBr<sub>3</sub> lattice, facilitating some lattice distortions and creating corresponding non-radiative recombination centers resulting in faster PL decay profiles (Fig. 3f) observed in such ambient environments.<sup>62–65</sup>

These experimental findings (Fig. 3c–h) highlight the strong susceptibility of CsMnBr<sub>3</sub> films to ambient conditions (involving moisture and oxygen) and underscores the necessity of encapsulation or passivation strategies to enable long-term device functionality of these films.<sup>66–70</sup> We also emphasize that these PL measurements were conducted without incorporating any surface coating or encapsulation strategies, and hence, they only reflect the unprotected, intrinsic stability of the as-fabricated CsMnBr<sub>3</sub> films under ambient conditions (*T*: ~17 °C, RH: ~65%). Similar degradation pathways have been extensively reported for different halide perovskites, such as MAPbI<sub>3</sub> and CsPbBr<sub>3</sub>, where water ingress and subsequent hydrate formation induce structural collapse and severe luminescence quenching behavior.<sup>71,72</sup> However, several strategies have been previously reported for similar halide perovskite systems to enhance their long-term ambient durability.<sup>73,74</sup> For instance, silica (SiO<sub>2</sub>) coatings have been widely utilized to shield perovskite nanocrystals from moisture- and oxygen-induced degradations,<sup>75</sup> while amidinium-based molecular passivation layers were recently employed for perovskite systems to dramatically enhance the environmental robustness, showing ~10-fold reduction in ligand deprotonation and ~2-fold increase in retention of the photoluminescence quantum yield under ambient conditions.<sup>76</sup> Overall, such encapsulation strategies can offer realistic pathways to enhance the long-term



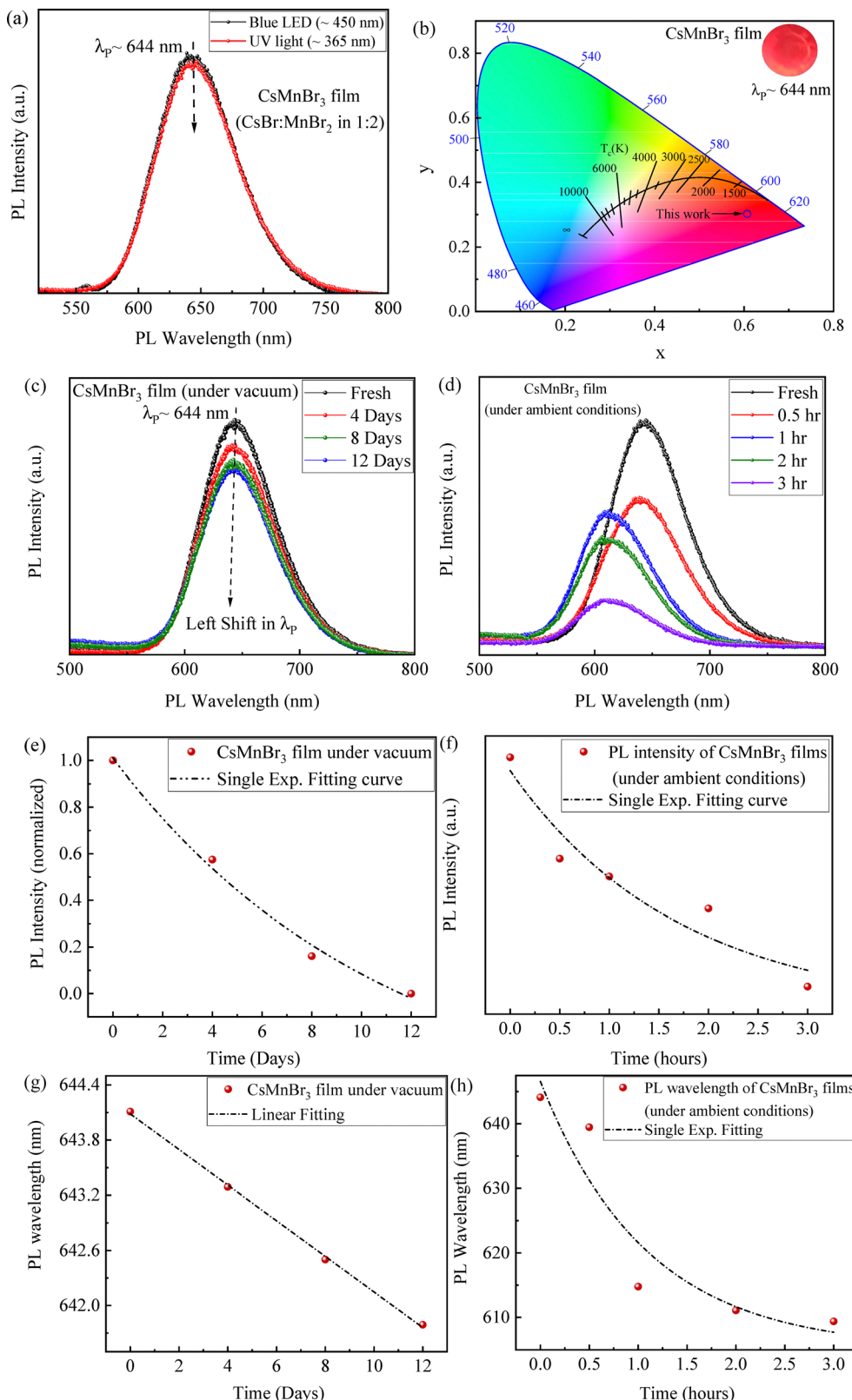


**Fig. 3** (a) PL spectra of CsMnBr<sub>3</sub> films under different excitation sources, (b) CIE chromaticity diagram of red-emitting CsMnBr<sub>3</sub> films, (c), (e) and (g) long-term stability curves of CsMnBr<sub>3</sub> films stored under vacuum conditions, and (d), (f) and (h) long-term stability curves of CsMnBr<sub>3</sub> films exposed to ambient conditions ( $T: \sim 17$  °C, RH:  $\sim 65\%$ ).

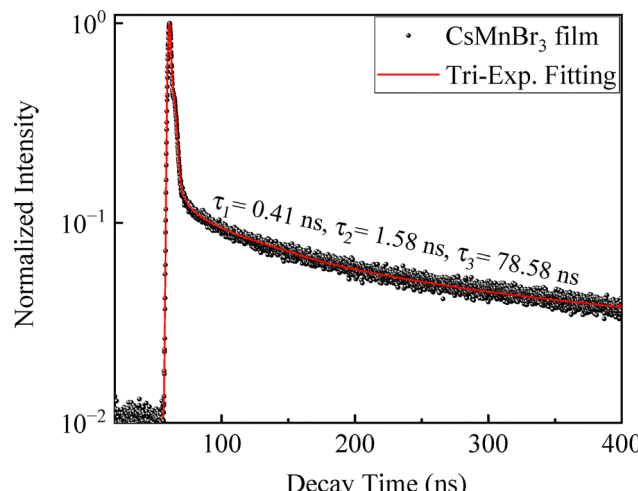


Fig. 4 Transient PL decay curves of the as-prepared  $\text{CsMnBr}_3$  films fitted with the tri-exponential decay equation.

stability of the as-synthesized  $\text{CsMnBr}_3$  films for practical optoelectronic and display applications.<sup>73,74</sup>

The charge-carrier recombination dynamics of the as-prepared  $\text{CsMnBr}_3$  films was probed using time-resolved photoluminescence spectroscopy (TRPL). Fig. 4 presents the temporal profile of TRPL for the  $\text{CsMnBr}_3$  films with the PL emission peak centered around  $\sim 644$  nm. The temporal profile of TRPL is fitted using a tri-exponential decay equation given as:<sup>77,78</sup>

$$I_{\text{TRPL}}(t) = A_1 e^{-t/\tau_1} + A_2 e^{-t/\tau_2} + A_3 e^{-t/\tau_3} \quad (1)$$

here, ' $A_i$ ' ( $i = 1, 2$  and  $3$ ) represents the relative amplitudes, and ' $\tau_i$ ' represents the characteristic lifetime of the  $i$ th component, respectively.

The curve fitting reveals three distinct characteristic lifetimes of  $78.58$  ns,  $1.58$  ns and  $0.41$  ns, corresponding to radiative recombination, surface-mediated recombination and trap-mediated recombination processes, respectively.<sup>78</sup> The longer radiative carrier lifetime component of  $\sim 78$  ns for the  $\text{CsMnBr}_3$  films, compared to previously reported decay components for different perovskite systems such as  $\text{CsPbBr}_3$  and  $\text{MAPbI}_3$ ,<sup>4,15,79,80</sup> indicates strong suppression of non-radiative recombination channels that are typically introduced *via* surface defects or trap states,<sup>78</sup> and points towards an effective defect passivation within these films. Additionally, the longer radiative lifetime components in halide perovskite systems, such as  $\text{CsMnX}_3$ ,  $\text{CsPbX}_3$  and  $\text{MAPbX}_3$ , are generally associated with higher internal quantum yield (QY) and improved device performance in opto-electronic applications, such as LEDs and other photovoltaics systems.<sup>81,82</sup> The mechanism behind such prolonged radiative decays is usually ascribed to an array of factors, including low defect density, reduced electron-phonon coupling, and possible charge carrier localization.<sup>83,84</sup>

The temperature dependence of photoluminescence was investigated for the as-prepared  $\text{CsMnBr}_3$  films, using the PL spectra shown in Fig. 5a, under ambient conditions and

$\sim 365$  nm UV irradiation. The temperature was slowly increased from  $\sim 20$  °C to  $\sim 120$  °C. A decrease in PL intensity with increasing temperature was observed (Fig. 5b), which can be ascribed to enhanced exciton-phonon dissociation<sup>85</sup> from a higher degree of scattering at elevated temperatures, resulting in alteration of charge carrier's effective masses and ultimately reducing the radiative recombination rates.<sup>85</sup> Such thermal quenching of photoluminescence is a common phenomenon for most luminescent materials, including perovskites of  $\text{CsPbX}_3$ <sup>4,86,87</sup> and  $\text{CsMnX}_3$ .<sup>44,85,88,89</sup> The temperature-dependent PL behavior can be approximately described using the following equation,<sup>85,88,89</sup>

$$I(T) = \frac{I(0)}{1 + Be^{-E_a/k_b T}} \quad (2)$$

where  $I(T)$  and  $I(0)$  are the PL peak intensities at temperatures of  $T$  and  $0$  K, respectively,  $B$  is a constant,  $k_b$  is the Boltzmann constant, and  $E_a$  is the activation energy.

Using eqn (2) to curve-fit the data in Fig. 5b yields a thermal activation energy of  $\sim 141$  meV, which is significantly higher than some previously reported values for halide perovskite systems, including  $\text{CsPbBr}_3$  ( $\sim 14$ – $75$  meV),<sup>90,91</sup>  $\text{MAPbX}_3$  ( $\sim 6$ – $53$  meV),<sup>92</sup>  $\text{Cs}_3\text{BiBr}_6$  ( $\sim 41$  meV),<sup>93</sup> and  $\text{MAPb}(\text{Br}_{x}\text{I}_{1-x})_3$  ( $\sim 20$ – $38$  meV).<sup>94</sup> A higher energy barrier reduces an overall thermal accessibility of non-radiative decay pathways, suggesting stronger confinement of the emitting centers and fewer trap-mediated recombination losses. This behavior aligns with the localized nature of  $\text{Mn}^{2+}$  d-d characteristic transitions in  $[\text{MnBr}_6]$  octahedra present inside the  $\text{CsMnBr}_3$  lattice, making them less susceptible to phonon-mediated thermal scattering compared to the delocalized band-edge excitons in Pb-based perovskite systems.<sup>95</sup>

Having a Br-rich environment during the synthesis of  $\text{CsMnBr}_3$  films may facilitate surface passivation *via* improving surface coordination by saturating under-coordinated metal sites, increasing the thermal energy barrier for non-radiative recombination channels.<sup>96,97</sup> For instance, Ghimire *et al.*<sup>96</sup> demonstrated enhancement in luminescence behavior (such as PLQY of  $\sim 98\%$ ) of  $\text{CsPbBr}_3$  perovskite by filling Br-vacancies with  $\text{NaBr}$ ,  $\text{KBr}$  and  $\text{CsBr}$  halides, resulting in a reduction of non-radiative decay rates. Similarly, Jing *et al.*<sup>97</sup> developed a Br-rich passivation layer *via* selective etching in mixed halide  $\text{CsPb}(\text{Br}_{x}\text{I}_{1-x})_3$  perovskite, enhancing the PL intensity by  $\sim 10^3$  times and suppressing non-radiative decay pathways through this passivation layer.

The temperature-dependent PL spectrum of the  $\text{CsMnBr}_3$  films shows a linear monotonous blue shift in the PL emission peak with increasing temperature in accordance with eqn (S3) in the SI<sup>85</sup>. The decreasing rate of the PL peak wavelength with respect to temperature is  $\sim 0.024$  nm K $^{-1}$  from the linear regression fitting. This blue shift is usually attributed to an interplay of lattice expansion, exciton-phonon coupling, and possible modifications in self-trapped exciton (STE) states, which effectively shift the dominant PL emission to higher energy states as temperature increases.<sup>64</sup>–<sup>67</sup> A similar behavior

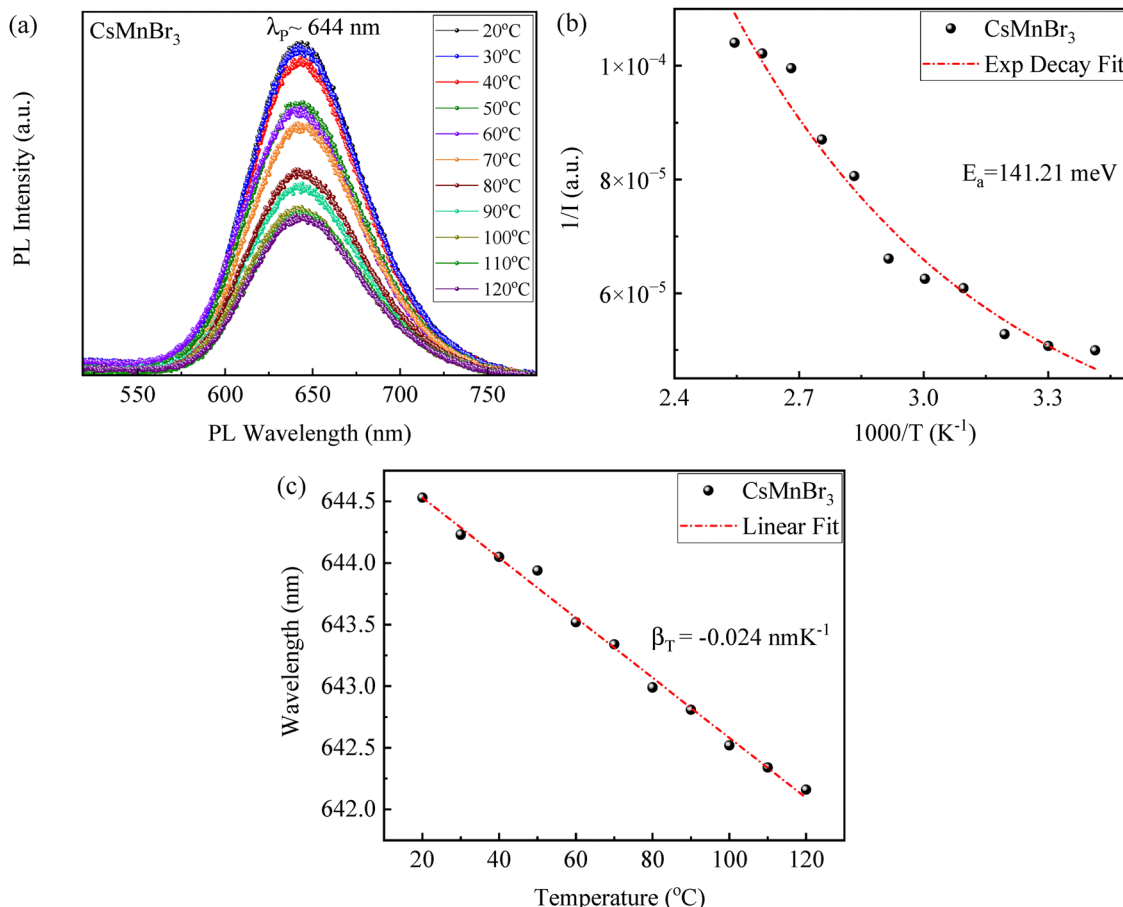


**Fig. 5** (a) PL spectra of the as-prepared CsMnBr<sub>3</sub> films at different temperatures, (b) temperature dependence of PL peak intensity, and (c) temperature dependence of PL peak wavelength.

has already been observed for many halide perovskite materials, including CsMnBr<sub>3</sub> and CsPbBr<sub>3</sub>.

The electrical response of the as-prepared CsMnBr<sub>3</sub> films was evaluated under different illumination conditions, including dark, white light, and UV light ( $\lambda$ :  $\sim 365$  nm) at varying excitation intensities, as shown in Fig. 6a-d, respectively. Fig. 6a shows the current-voltage ( $I$ - $V$ ) characteristics of these films under white, dark and UV excitations at a scan rate of  $0.55$  V s<sup>-1</sup>. The linear  $I$ - $V$  response points towards ohmic contacts between electrodes and the film, enabling the extraction of conductance using eqn (S4) shown in the SI.<sup>98,99</sup> The conductance values for these films decrease progressively under dark ( $G$ :  $\sim 2.06 \times 10^{-9}$  S) to white light ( $G$ :  $\sim 1.69 \times 10^{-9}$  S) and to UV light ( $G$ :  $\sim 9.6 \times 10^{-10}$  S) illumination conditions, with the lowest conductance value ( $G$   $\sim 9.6 \times 10^{-10}$  S) under the UV irradiation. This indicates the presence of negative photoconductivity (NPC)<sup>100-102</sup> inside the as-synthesized CsMnBr<sub>3</sub> films and is consistent with some recent reports on other perovskite materials, including CsPbX<sub>3</sub>, Cs<sub>3</sub>Bi<sub>2</sub>Br<sub>9</sub>, and Cs<sub>3</sub>Bi<sub>2</sub>Cl<sub>9</sub>.<sup>100-102</sup>

For instance, Tailor *et al.*<sup>101</sup> observed a linear  $I$ - $V$  response for the Cs<sub>3</sub>Bi<sub>2</sub>Br<sub>9</sub> crystal, whose conductivity decreases under light exposure in comparison to the 'dark' state, exhibiting

negative photoconductivity (NPC) due to trap of photo-generated charge carriers at charged defect states and an internal electric field opposite to the externally applied field, leading to a decrease of the net current under light illumination. Similarly, the time-resolved current-time ( $I$ - $t$ ) measurements conducted on these films show a linear  $I$ - $t$  behavior with the change rate of current ( $r$ ) (extracted *via* eqn (S5) in the SI) exhibiting a similar decreasing behavior from the dark ( $r$ :  $\sim 1.21 \times 10^{-9}$  A s<sup>-1</sup>) to white light ( $r$ :  $\sim 9.95 \times 10^{-10}$  A s<sup>-1</sup>) to UV light ( $r$ :  $\sim 5.6 \times 10^{-10}$  A s<sup>-1</sup>) (Fig. S2a in the SI). The lowest change rate is  $\sim 5.6 \times 10^{-10}$  A s<sup>-1</sup> under UV light, consistent with the suppressed carrier transport observed in the  $I$ - $V$  curves shown in Fig. 6a.

To further investigate the behavior of negative photoconductivity (NPC), the electrical response of the as-prepared films was observed under varying UV intensities of  $0.01$  W cm<sup>-2</sup> (UV<sub>1</sub>),  $0.03$  W cm<sup>-2</sup> (UV<sub>2</sub>),  $0.14$  W cm<sup>-2</sup> (UV<sub>3</sub>), and  $0.57$  W cm<sup>-2</sup> (UV<sub>4</sub>), as shown in Fig. 6b. Interestingly, the electrical conductance exhibits an intensity-dependent suppression (from  $\sim 2.06 \times 10^{-9}$  S under dark to  $\sim 5.82 \times 10^{-10}$  S under UV), with the highest UV illumination intensity yielding the lowest conductance ( $\sim 5.82 \times 10^{-10}$  S). Correspondingly, the  $I$ - $t$  curves under the corresponding UV illumination intensities

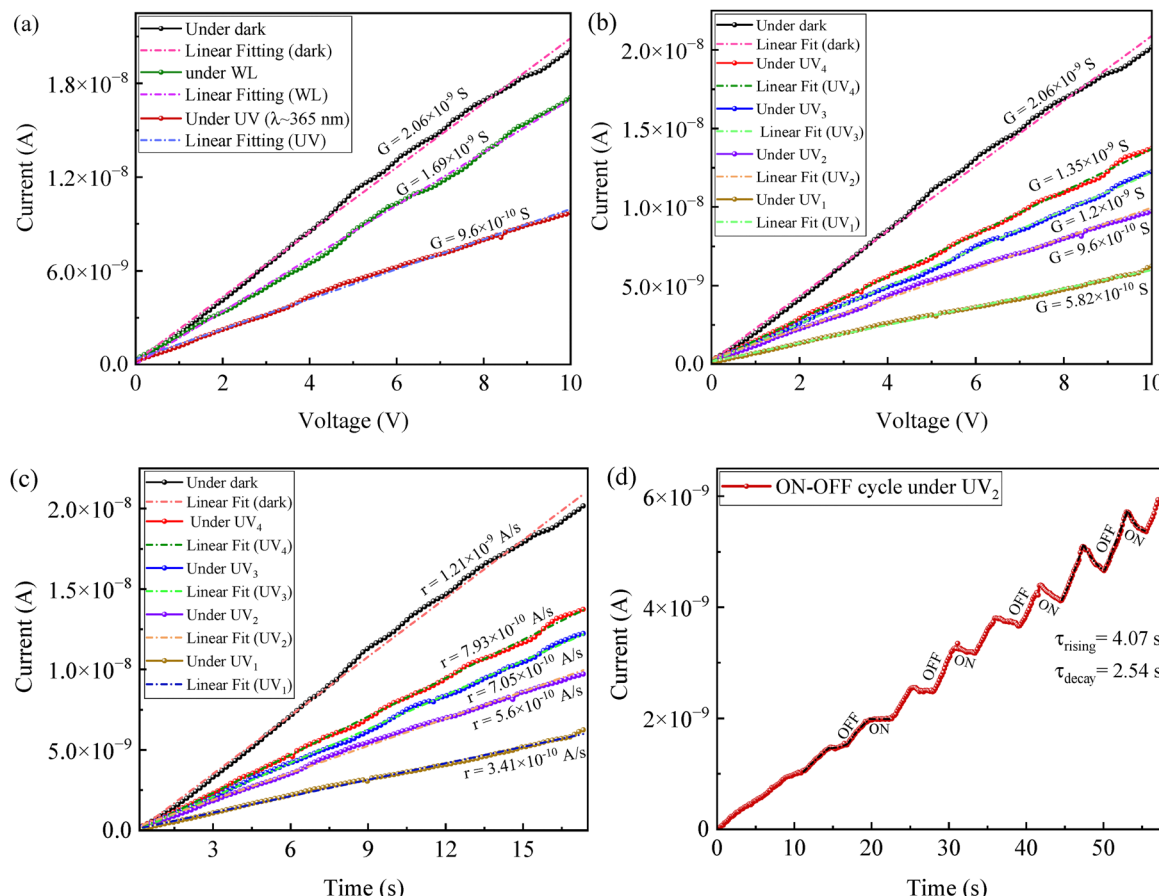


**Fig. 6** (a) Current–voltage ( $I$ – $V$ ) characteristics of the as-prepared  $\text{CsMnBr}_3$  films under dark, white light, and UV light ( $\lambda: \sim 365 \text{ nm}$ ) at a scan rate of  $0.55 \text{ V}\cdot\text{s}^{-1}$ , (b)  $I$ – $V$  curves under UV light with different intensities ( $0.57 \text{ W cm}^{-2}$ ,  $0.14 \text{ W cm}^{-2}$ ,  $0.03 \text{ W cm}^{-2}$ , and  $0.01 \text{ W cm}^{-2}$ ) at a scan rate of  $0.55 \text{ V}\cdot\text{s}^{-1}$ , (c)  $I$ – $t$  curves of the as-prepared  $\text{CsMnBr}_3$  films under UV light ( $\lambda: \sim 365 \text{ nm}$ ) of different intensities at a scan rate of  $0.55 \text{ V}\cdot\text{s}^{-1}$ , and (d)  $I$ – $t$  response under UV-assisted ON–OFF cycles at a scan rate of  $0.25 \text{ V}\cdot\text{s}^{-1}$ , demonstrating negative photoconductivity (NPC).

(UV<sub>1</sub> to UV<sub>4</sub>) (Fig. 6c) reveal a decreasing trend in the change rate of current ( $r$ ) with increasing UV intensity, consistent with the  $I$ – $V$  results. The observed trends are consistent with trap-mediated mechanisms,<sup>100–103</sup> where higher excitation intensities (such as UV irradiation) can promote carrier capture at surface defects, grain boundaries, and other photoactive sites within the micron-sized, powder-like  $\text{CsMnBr}_3$  films, thereby reducing free carrier density and transport efficiency, leading to NPC behavior. However, we note that direct dynamic measurements, such as time-resolved photoluminescence (TRPL), temperature-dependent carrier transport, or power-dependent lifetime studies, would be required to unambiguously confirm this NPC mechanism, however, similar NPC responses, attributed to trap activation, space-charge buildup, and light-induced defect occupations, have been widely reported in other halide perovskite systems including  $\text{CsPbX}_3$ ,  $\text{Cs}_3\text{Bi}_2\text{Br}_9$ , and  $\text{Cs}_3\text{Bi}_2\text{Cl}_9$ , respectively.<sup>100–103</sup>

Fig. S2b in the SI shows the  $I$ – $V$  response of the as-prepared  $\text{CsMnBr}_3$  films during ON–OFF alternate cycling under UV illumination ( $\lambda: \sim 365 \text{ nm}$ ) at a scan rate of  $0.25 \text{ V}\cdot\text{s}^{-1}$ . Electric current exhibits an approximately exponential rise when transitioning to the dark ('OFF') state and a corresponding

exponential decay under UV ('ON') illumination. These effects become more pronounced at higher applied voltages. Correspondingly, Fig. 6d displays the  $I$ – $t$  response for the ON–OFF cycles, showing well-defined transient behavior. Fitting these  $I$ – $t$  curves with a single-exponential equation (eqn (S6)<sup>104</sup> in the SI) yields a rise characteristic time ( $\tau_{\text{rise}}$ ) of  $\sim 4.07 \text{ s}$  and a decay characteristic time ( $\tau_{\text{decay}}$ ) of  $\sim 2.54 \text{ s}$ . Interestingly, despite the larger value of  $\tau_{\text{rise}}$  than the  $\tau_{\text{decay}}$ , the overall 'dark' current after each 'OFF' cycle recovered to progressively higher values than the previous baseline, indicating an effective and relatively faster self-recovery process, as shown in Fig. 6d. This is in contrast to other NPC materials, for instance, Tailor *et al.*<sup>101</sup> reported slower  $I$ – $t$  response curves with an overall decaying current for  $\text{Cs}_3\text{Bi}_2\text{Br}_9$  during ON–OFF cycling under highly intense light exposure ( $100 \text{ mW cm}^{-2}$ ).

The practical applicability of the as-prepared  $\text{CsMnBr}_3$  films was demonstrated by constructing a white-emitting backlight structure from the red-emitting  $\text{CsMnBr}_3$  and green-emitting  $\text{CsPbBr}_3$  films with a commercial blue LED source ( $\lambda: \sim 450 \text{ nm}$ ), as schematically illustrated in Fig. S4 in the SI. Upon excitation, the backlight structure exhibits distinct and well-separated PL emission peaks corresponding to blue ( $\sim 450 \text{ nm}$ ), green ( $\sim 524 \text{ nm}$ ),



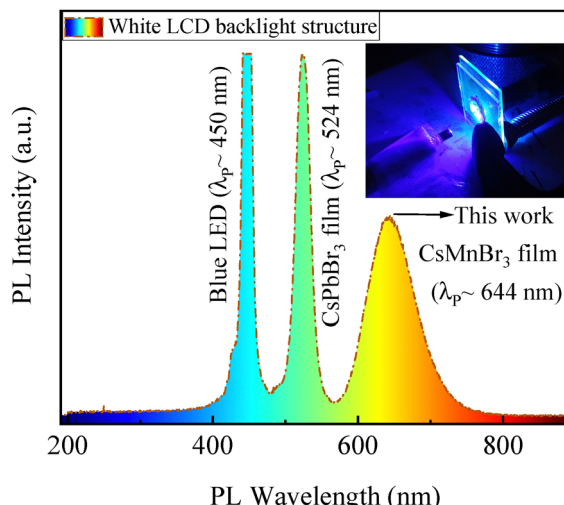


Fig. 7 PL response of the as-constructed white-emitting backlight structure showing distinct blue ( $\sim 450$  nm), green ( $\sim 524$  nm), and red ( $\sim 644$  nm) emission peaks with the inset depicting an optical image of the backlight structures under dark.

and red ( $\sim 644$  nm) components, as shown in Fig. 7. The inset in Fig. 7 depicts an optical image of the constructed structure under dark, confirming the production of bright white light through color mixing of RGB components. Such clear spectral resolution of RGB components is highly beneficial for achieving wide color gamut coverage and superior color rendering in display applications (discussed later in this paper), and aligns with the recent drive toward perovskite-based backlighting technologies for next-generation optoelectronic devices.<sup>105,106</sup>

## 4. Discussion

In this work,  $\text{CsMnBr}_3$  films were deposited on the Cu substrate at  $\sim 50$  °C from an aqueous solution of  $\text{CsBr}$  and  $\text{MnBr}_2$ . The XRD pattern (Fig. 2f) reveals small traces of impurities of  $\text{CuBr}_2$  and  $\text{MnO}_2$ , suggesting the following reaction



In principle, water plays a crucial and active role in the synthesis of  $\text{CsMnBr}_3$  instead of just serving as a passive solvent. The presence of even small amounts of water significantly enhances ionic mobility and cation-halide ( $\text{Mn}^{2+}$ – $\text{Br}^-$ ) interaction, facilitating the formation of well-defined  $[\text{MnBr}_6]^{4-}$  octahedral coordination, and accelerating perovskite formation. This effect has been demonstrated by Tsvetkov *et al.*<sup>107</sup> in the mechano-chemical synthesis of similar halide perovskite materials, such as  $\text{CsPbI}_3$ , where water was demonstrated to strongly promote the reaction kinetics of  $\text{CsPbI}_3$  from  $\text{CsI}$  and  $\text{PbI}_2$  mixtures *via* increased mobility of the constituting ionic species. Additionally, Xiao *et al.*<sup>108</sup> demonstrated a nuanced role of water in crystallization of the  $\text{MAPbI}_3$  perovskite. They reported that a suitable water content can facilitate high-quality perovskite film growth by enabling intermediate hydrate

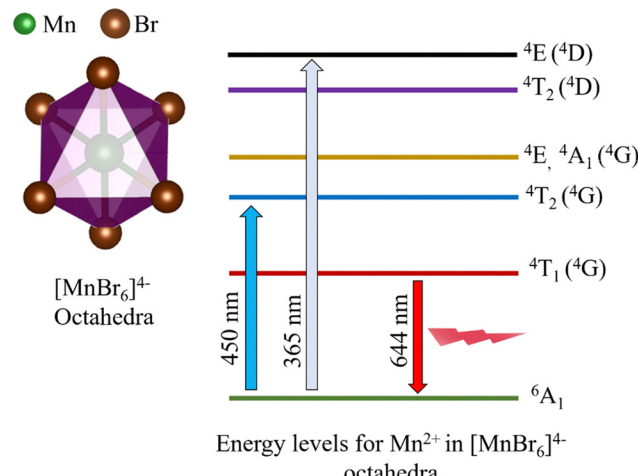


Fig. 8 Energy level diagram of octahedrally coordinated  $\text{Mn}^{2+}$  ions in  $\text{CsMnBr}_3$ , depicting d-d transitions and the photoluminescence pathway for red emission ( $\sim 644$  nm).

formation such as  $\text{MAPbI}_3 \cdot \text{H}_2\text{O}$ , facilitating the conversion process from precursors to perovskite structures.

In the  $\text{CsMnBr}_3$  lattice, the  $\text{Mn}^{2+}$  ion is octahedrally coordinated with  $\text{Br}^-$  anions to form  $[\text{MnBr}_6]^{4-}$  octahedra (Fig. 8), which is responsible for the observed red PL emission ( $\sim 644$  nm) (Fig. 2g), owing to the d-d transition of  $\text{Mn}^{2+}$  cations from  ${}^4\text{T}_1$  ( ${}^4\text{G}$ ) to  ${}^6\text{A}_1$  energy states (Fig. 8) and this is further verified by exciting the lattice with two different high-energy sources ( $\sim 365$  nm and  $\sim 450$  nm) (Fig. 3a) resulting in similar red PL emission ( $\sim 644$  nm with FWHM of  $\sim 7$  nm), consistent with previous reports on  $\text{CsMnBr}_3$ .<sup>46,47</sup> Almutlaq *et al.*<sup>15</sup> concluded that the red PL emission ( $\sim 643$  nm) of  $\text{CsMnBr}_3$  is indeed due to  ${}^4\text{T}_1$  to  ${}^6\text{A}_1$  (d-d) transitions of  $\text{Mn}^{2+}$  in  $[\text{MnBr}_6]$  octahedra after extracting a similar red PL emission ( $\sim 643$  nm with FWHM of  $\sim 78$  nm) under three different excitation wavelengths ( $\sim 380$  nm,  $\sim 45$  nm, and  $\sim 540$  nm). Furthermore, a relatively modest photoluminescence quantum yield (PLQY  $\sim 30\%$ ) in our  $\text{CsMnBr}_3$  films (particle size  $\sim 0.6$   $\mu\text{m}$ ), compared to  $\text{CsMnBr}_3$  nanocrystals (PLQY  $\sim 54\%$ ) reported by Almutlaq *et al.*<sup>15</sup> may be attributed to an array of factors including strong light scattering and re-absorption arising from the micron-sized powder morphology compared to the nanocrystalline systems reported in past literature,<sup>15,17</sup> residual impurity phases and surface/bulk defect states, acting as nonradiative recombination centers, and partial oxidation of  $\text{Mn}^{2+}$  cations under ambient air, overall leading to a quenched photoluminescence behavior in Mn-based halide materials.<sup>109</sup>

Fig. 9 shows the temperature dependence of the band gap of the as-prepared  $\text{CsMnBr}_3$  films, which follows the Bose-Einstein model<sup>110</sup> given as:

$$E(T) = E_0(T) - \frac{2a}{e^{b/T} - 1} \quad (4)$$

where  $E_0(T)$  represents the band gap at 0 K,  $a$  describes the strength of the electron-phonon interaction, and  $b$  is the

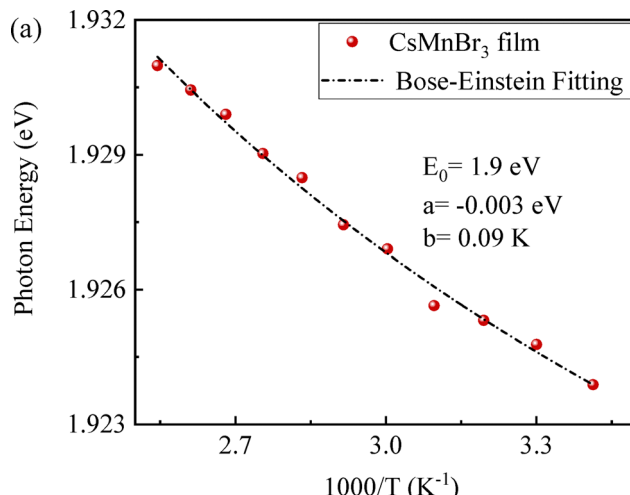


Fig. 9 Temperature dependence of photon energy for  $\text{CsMnBr}_3$  films, fitted via the Bose–Einstein model.

characteristic temperature linked to average photon energy, respectively.

The blue shift of the band gap with increasing temperature indicates higher electron–phonon activity and thermal lattice expansion at elevated temperatures, likely reducing the anti-bonding overlap between 3d Mn and 4p Br orbitals and ultimately widening the band gap. A similar behavior is reported for different halide perovskites, such as  $\text{CsPbBr}_3$ . Higher temperatures lead to enhanced electron–phonon scattering, resulting in lower antibonding overlap between 6s Pb and 4p Br, thereby shifting the valence band maxima (VBM) to lower energy values, and ultimately leading to a shift of PL emission peaks to higher energy values.<sup>86,95,111–114</sup>

The correlations between electronic conductance ( $G$ ) and irradiance ( $I$ ) and between photo-resistance ( $\Delta R_{\text{ph}}$ ) and UV-light intensity can be expressed as:

$$G = G_0 I^a \quad \text{and} \quad \Delta R_{\text{ph}} = R_0 I^b \quad (5)$$

where ' $G_0$ ' and ' $R_0$ ' represent the amplitude factors, and ' $a$ ' and ' $b$ ' represent the power law exponents, respectively. Fig. 10a and b presents the variations of electronic conductance and photo-resistance with irradiance as well as the fitting curves obtained using the power law relations in eqn (5).

The power-law dependence of electronic conductance and photo-resistance indicates that a strong UV irradiation enhances the trapping and/or recombination of charge carriers, limiting photocarrier migration, consistent with the observed NPC phenomena (Fig. 6a–d). Although direct defect characterization (such as EPR or XPS) or humidity-dependent photoconductivity studies were not conducted in present work, the observed NPC phenomena can plausibly be attributed to an array of defect-mediated charge-trapping mechanisms including the hygroscopic nature of  $\text{MnBr}_2$  facilitating rapid moisture uptake<sup>115</sup> (*via* formation of hydrates or other bromide complexes) and activating new deep trap states or ionic defects which can trap the charge carriers,<sup>57,116</sup> higher surface area or

powdered morphology exhibited by our as-synthesized  $\text{CsMnBr}_3$  films, which may enhance the recombination ‘hot spots’ for charge carriers, and UV activation of meta-stable trap states that may capture the photogenerated carriers, thereby impeding the overall carrier transport.<sup>100–102,117–119</sup>

Some related studies showed that in trap-rich systems, photoconductivity often transitions from linear to sub-linear behavior depending on trap-state density. For instance, Yi *et al.*<sup>120</sup> demonstrated that the photoconductivity of hybrid and all inorganic perovskite crystals exhibited a crossover in power law dependence with respect to excitation intensities between power exponents 1 (linear) and 1/2 (sublinear). This behavior was observed in all compounds of cation type (organic or inorganic) or crystallographic phases.

The photocurrent–voltage ( $\Delta I_{\text{ph}}-V$ ) curves exhibit an initial linear region followed by a nonlinear threshold ( $V_{\text{NL}}$ ) that shifts to higher voltage values with increasing irradiance, as shown in Fig. 10c. The slopes of the linear region of these  $\Delta I_{\text{ph}}-V$  curves show a decaying trend with increasing excitation intensities, as fitted via the following equation:<sup>121</sup>

$$\Delta I_{\text{ph}} = cV + d \quad (6)$$

where ‘ $\Delta I_{\text{ph}}$ ’ represents the photo-current, ‘ $c$ ’ represents the slope of  $\Delta I_{\text{ph}}-V$  curves, and ‘ $d$ ’ represents the intercept of  $\Delta I_{\text{ph}}-V$  curves referring to the initial photocurrent values, respectively. Such a behavior further highlights the decaying behavior of photoconductance with increasing excitation intensities, consistent with the NPC behavior of the films (Fig. 10b). Correspondingly, the time-resolved photocurrent ( $\Delta I_{\text{ph}}-t$ ) traces also mirror similar results with diminishing slopes over time with increasing excitation intensities, as shown in Fig. S2c in the SI. These trends strongly reflect trap-mediated conduction behavior for the  $\text{CsMnBr}_3$  films, where higher biases and longer times are needed to overcome the immobilization of carriers by deep trap states.

The analysis of the change rates of current ( $r$ ) and photocurrent ( $\Delta r_{\text{ph}}$ ), as shown in Fig. 10d and e, demonstrates an irregular decaying trend of the change rate of current with excitation irradiance. The change rate of photocurrent ( $\Delta r_{\text{ph}}$ ) follows a power-law decaying model ( $\Delta r_{\text{ph}} = r_0 I^\alpha$ )<sup>120</sup> with  $\alpha \sim 0.2$ , implying diminishing gains at higher photon flux levels. The photocurrent at  $V_{\text{NL}}$  (onset of non-linear region) continues to decline with excitation intensity following a power-law model ( $\Delta I_{\text{ph}} = s_0 I^\beta$ ),<sup>120</sup> as shown in Fig. 10f, with  $\beta \sim 0.19$ , consistent with other perovskite materials of  $\text{CH}_3\text{NH}_3\text{PbBr}_3$  and  $\text{CsPbBr}_3$ , where photocurrent exhibited a power dependence with incident excitation intensities with a crossover between power exponents of 1 and 1/2, respectively.<sup>120</sup> These results highlight the trapping of photo-generated charge carriers *via* different trap states, leading to NPC behavior of the  $\text{CsMnBr}_3$  films.

The as-constructed white emitting backlight structures (Fig. 7) exhibit a ‘colder’ white light with a higher color coordinated temperature (CCT) of  $\sim 8455$  K and a wider color gamut coverage area (extracted through Commission Internationale de l’Eclairage (CIE) color coordinates) spanning 132% of NTSC 1953 and  $\sim 186\%$  of sRGB color standards,



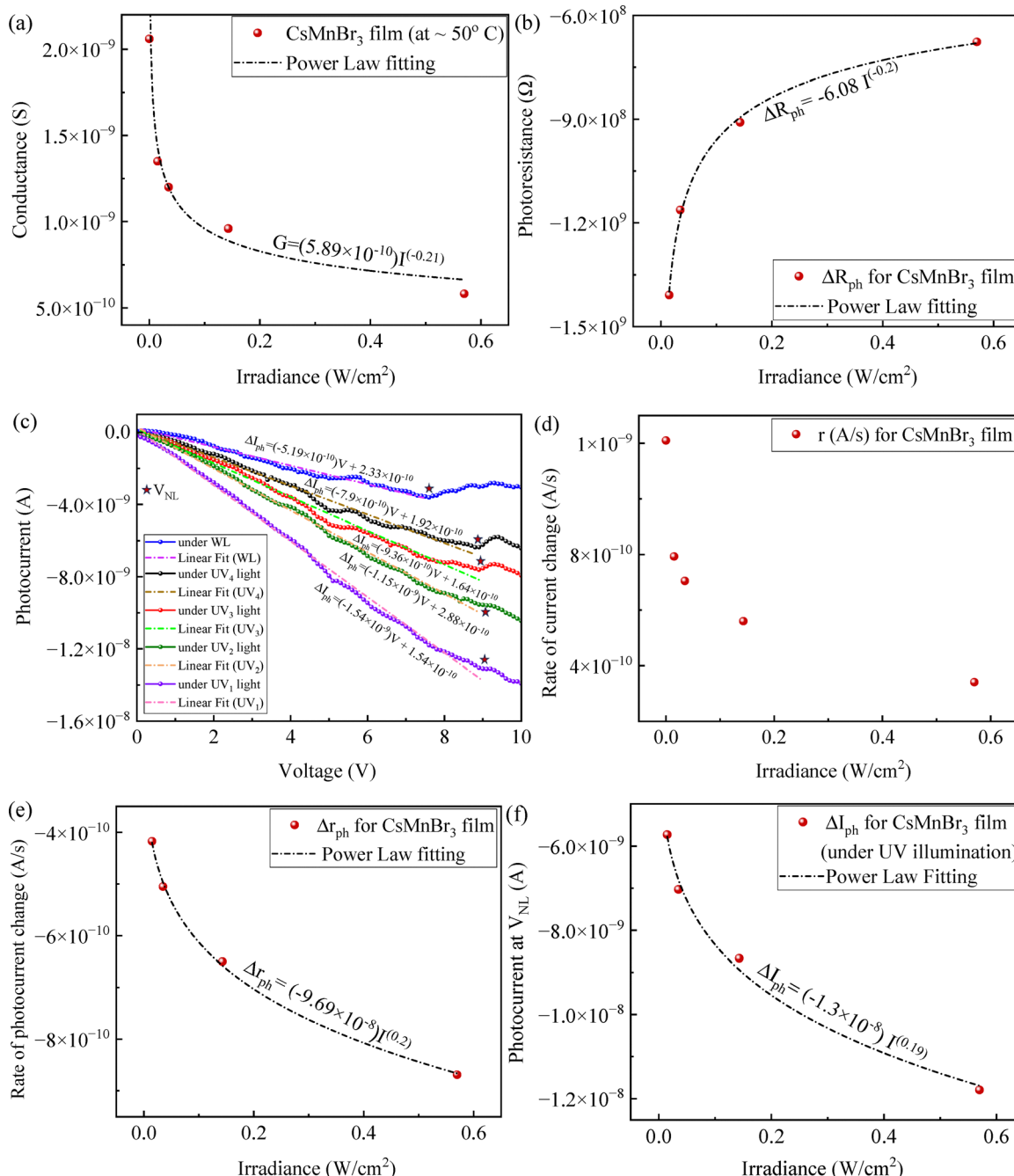


**Fig. 10** Electrical and photo-response characteristics of  $\text{CsMnBr}_3$  films under UV ( $\sim 365$  nm) irradiation: (a) conductance as a function of UV irradiance, (b) photoresistance as a function of UV irradiance, (c) photocurrent–voltage characteristics, (d) change rate of current as a function of UV irradiance, (e) change rate of photocurrent as a function of irradiance, and (f) photocurrent at  $V_{\text{NL}}$  (onset of the non-linear region) as a function of irradiance.

as calculated *via* eqn (S7) and (S8)<sup>85</sup> and depicted in Fig. 11, respectively. Although the spectral overlaps between emission bands were not separately integrated, it was inherently represented in the measured combined PL spectrum for these stacked LCD backlight structures (Fig. 7). Furthermore, these wide gamut coverage values exceed those commonly reported for red-emitting phosphor films<sup>18,85,122</sup> (commonly used in white backlight structures), underscoring not only the superior spectral purity but also the color rendering capability of the

$\text{CsMnBr}_3$  films. When coupled with the environmentally benign aqueous synthesis route, it further highlights the promise of these green-fabricated  $\text{CsMnBr}_3$  films for next-generation display technologies.

Comparison among different red emitting phosphors,<sup>123–136</sup> utilized in white LCD backlight structures, is made in terms of the CIE color gamut coverage area with respect to the NTSC standard, as shown in Fig. 12. It is evident that the red-emitting  $\text{CsMnBr}_3$  films outperform other red-emitting phosphors reported,

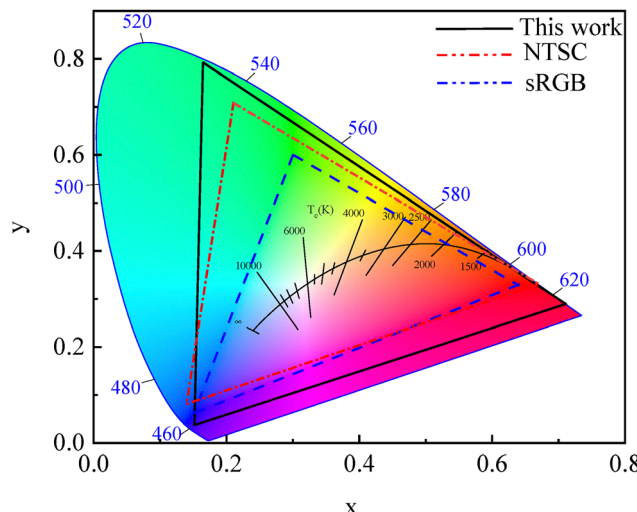


Fig. 11 CIE color gamut coverage of white emitting backlight structures from the as-prepared  $\text{CsMnBr}_3$  films ( $\lambda_p \sim 644$  nm).

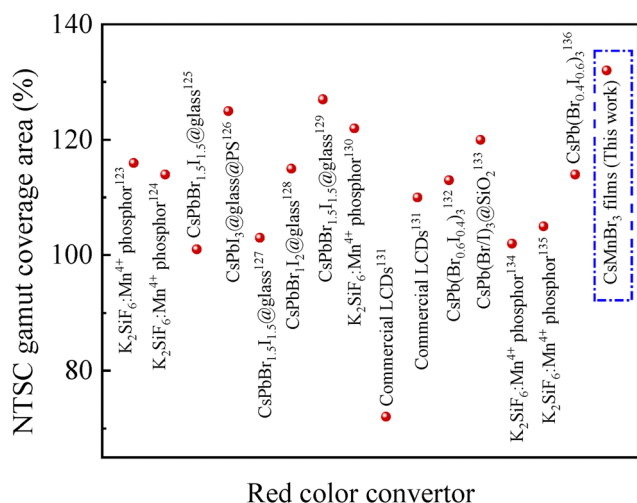


Fig. 12 Relative NTSC gamut coverage areas of white-emitting backlight structures with different green emitting films.

making them excellent candidates for next generation display applications.

## 4. Conclusions

In summary, we have demonstrated a sustainable, facile, and low-cost approach to synthesize red-emitting  $\text{CsMnBr}_3$  films of high quality by using water as the only solvent. This low temperature green route overcomes the limitations of conventional methods that rely on toxic solvents, high temperatures, and/or high inert atmospheres, and directly yields emissive thin films rather than powders or colloidal nanocrystals. The as-fabricated  $\text{CsMnBr}_3$  films exhibit efficient deep-red photoluminescence ( $\lambda \sim 644$  nm) and an exceptionally wide color gamut (spanning  $\sim 132\%$  of NTSC 1953 and  $\sim 186\%$  of sRGB color standards), underscoring their suitability as next-generation

backlight materials for wide-color displays, which majorly rely on red phosphors to date. These films exhibit an intriguing NPC behavior and power-law dependent photo-responses, which provide new insights into the charge transport mechanism of Pb-free Mn-based halide perovskites. Overall, this work offers fresh insights for scalable, environment-friendly, and high-performance phosphor films for optoelectronic and display technologies.

## Conflicts of interest

The authors declare no competing financial interest.

## Data availability

All possible experimental and analysed results have been included in this manuscript and supplementary information (SI) explicitly. No other new data have been generated by any further experiments/analyses. Supplementary information is available. See DOI: <https://doi.org/10.1039/d5ma01256b>.

## Acknowledgements

FY is grateful for the support by the NSF through the CBET-2018411 monitored by Dr Nora F Savage.

## References

1. B. Conings, J. Drijkoningen, N. Gauquelin, A. Babayigit, J. D'Haen, L. D'Olieslaeger, A. Ethirajan, J. Verbeeck, J. Manca and E. Mosconi, Intrinsic thermal instability of methylammonium lead trihalide perovskite, *Adv. Energy Mater.*, 2015, **5**(15), 1500477.
2. Y. Dong, T. Qiao, D. Kim, D. Parobek, D. Rossi and D. H. Son, Precise control of quantum confinement in cesium lead halide perovskite quantum dots via thermodynamic equilibrium, *Nano Lett.*, 2018, **18**(6), 3716–3722.
3. A. Tiwari, N. S. Satpute, C. M. Mehare and S. Dhole, Challenges, recent advances and improvements for enhancing the efficiencies of ABX<sub>3</sub>-based PeLEDs (perovskites light emitting diodes): A review, *J. Alloys Compd.*, 2021, **850**, 156827.
4. S. Singh, X. Tang and F. Yang, Low-temperature synthesis of highly stable blue-emitting perovskite  $\text{CsPbBr}_3$  quantum dots, *J. Phys. Chem. C*, 2025, **129**(7), 3942–3950.
5. K. Chen, C. Wang, Z. Peng, K. Qi, Z. Guo, Y. Zhang and H. Zhang, The chemistry of colloidal semiconductor nanocrystals: From metal-chalcogenides to emerging perovskite, *Coord. Chem. Rev.*, 2020, **418**, 213333.
6. Y. Bai, M. Hao, S. Ding, P. Chen and L. Wang, Surface chemistry engineering of perovskite quantum dots: strategies, applications, and perspectives, *Adv. Mater.*, 2022, **34**(4), 2105958.
7. F. Zhang, H. Zhong, C. Chen, X.-G. Wu, X. Hu, H. Huang, J. Han, B. Zou and Y. Dong, Brightly luminescent and

color-tunable colloidal  $\text{CH}_3\text{NH}_3\text{PbX}_3$  ( $\text{X} = \text{Br}, \text{I}, \text{Cl}$ ) quantum dots: potential alternatives for display technology, *ACS Nano*, 2015, **9**(4), 4533–4542.

8 Y. Tong, E. Bladt, M. F. Aygüler, A. Manzi, K. Z. Milowska, V. A. Hintermayr, P. Docampo, S. Bals, A. S. Urban and L. Polavarapu, Highly luminescent cesium lead halide perovskite nanocrystals with tunable composition and thickness by ultrasonication, *Angew. Chem., Int. Ed.*, 2016, **55**(44), 13887–13892.

9 M. Chen, Y. Zou, L. Wu, Q. Pan, D. Yang, H. Hu, Y. Tan, Q. Zhong, Y. Xu and H. Liu, Solvothermal synthesis of high-quality all-inorganic cesium lead halide perovskite nanocrystals: from nanocube to ultrathin nanowire, *Adv. Funct. Mater.*, 2017, **27**(23), 1701121.

10 Q. Pan, H. Hu, Y. Zou, M. Chen, L. Wu, D. Yang, X. Yuan, J. Fan, B. Sun and Q. Zhang, Microwave-assisted synthesis of high-quality “all-inorganic”  $\text{CsPbX}_3$  ( $\text{X} = \text{Cl}, \text{Br}, \text{I}$ ) perovskite nanocrystals and their application in light emitting diodes, *J. Mater. Chem. C*, 2017, **5**(42), 10947–10954.

11 Z. Long, H. Ren, J. Sun, J. Ouyang and N. Na, High-throughput and tunable synthesis of colloidal  $\text{CsPbX}_3$  perovskite nanocrystals in a heterogeneous system by microwave irradiation, *Chem. Commun.*, 2017, **53**(71), 9914–9917.

12 L. Rao, Y. Tang, C. Song, K. Xu, E. T. Vickers, S. Bonabi Naghadeh, X. Ding, Z. Li and J. Z. Zhang, Polar-solvent-free synthesis of highly photoluminescent and stable  $\text{CsPbBr}_3$  nanocrystals with controlled shape and size by ultrasonication, *Chem. Mater.*, 2018, **31**(2), 365–375.

13 J. Zou, M. Li, X. Zhang and W. Zheng, Perovskite quantum dots: synthesis, applications, prospects, and challenges, *J. Appl. Phys.*, 2022, **132**(22), 220901.

14 M. H. Miah, M. U. Khandaker, M. J. Hossen, N. E. Ashrafi, I. Jahan, M. Shahinuzzaman, M. Nur-E-Alam, M. Y. Hanfi, M. H. Ullah and M. A. Islam, Lead-free alternatives and toxicity mitigation strategies for sustainable perovskite solar cells: a critical review, *Mater. Adv.*, 2025, **6**(9), 2718–2752.

15 J. Almutlaq, W. J. Mir, L. Gutiérrez-Arzaluz, J. Yin, S. Vasylevskyi, P. Maity, J. Liu, R. Naphade, O. F. Mohammed and O. M. Bakr,  $\text{CsMnBr}_3$ : Lead-free nanocrystals with high photoluminescence quantum yield and picosecond radiative lifetime, *ACS Mater. Lett.*, 2021, **3**(3), 290–297.

16 P. Gao, S. Cheng, J. Liu, J. Li, Y. Guo, Z. Deng, T. Qin and A. Wang, Facile synthesis of highly emissive all-inorganic manganese bromide compounds with perovskite-related structures for white LEDs, *Molecules*, 2022, **27**(23), 8259.

17 G. Xu, C. Wang, Y. Li, W. Meng, G. Luo, M. Peng, B. Xu and Z. Deng, Solid-state synthesis of cesium manganese halide nanocrystals in glass with bright and broad red emission for white LEDs, *Chem. Sci.*, 2023, **14**(20), 5309–5315.

18 J. H. Oh, H. Kang, M. Ko and Y. R. Do, Analysis of wide color gamut of green/red bilayered freestanding phosphor film-capped white LEDs for LCD backlight, *Opt. Express*, 2015, **23**(15), A791–A804.

19 S. Li, R.-J. Xie, T. Takeda and N. Hirosaki, Critical review—narrow-band nitride phosphors for wide color-gamut white LED backlighting, *ECS J. Solid State Sci. Technol.*, 2017, **7**(1), R3064.

20 L. Wang, X. Wang, T. Kohsei, K.-I. Yoshimura, M. Izumi, N. Hirosaki and R.-J. Xie, Highly efficient narrow-band green and red phosphors enabling wider color-gamut LED backlight for more brilliant displays, *Opt. Express*, 2015, **23**(22), 28707–28717.

21 D. Mo, L. Hu, G. Zeng, G. Chen, J. Wan, Z. Yu, Z. Huang, K. He, C. Zhang and M. Cheng, Cadmium-containing quantum dots: properties, applications, and toxicity, *Appl. Microbiol. Biotechnol.*, 2017, **101**(7), 2713–2733.

22 T. Zhao, S. Zhang and D. Zhu, A Novel Zero-Thermal-Quenching Red Phosphor with High Quantum Efficiency and Color Purity, *Inorganics*, 2023, **11**(10), 406.

23 M. Li, W. Li and H. Wei, Unique Optoelectronic Properties and Applications of Lead-Free Perovskites and Derivatives, *Adv. Photon. Res.*, 2025, **6**(2), 2400095.

24 P. Han, X. Zhang, C. Luo, W. Zhou, S. Yang, J. Zhao, W. Deng and K. Han, Manganese-doped, lead-free double perovskite nanocrystals for bright orange-red emission, *ACS Cent. Sci.*, 2020, **6**(4), 566–572.

25 T. W. Kang, E. J. Choi, Y. J. Park, J. Hwang, B. Bae and S. W. Kim, Phase-selective synthesis of lead-free  $\text{CsMnBr}_3$  and  $\text{Cs}_3\text{MnBr}_5$  nanocrystals dependent on solvent concentration, *Opt. Lett.*, 2022, **47**(7), 1806–1809.

26 H. Bahmani Jalali, A. Pianetti, J. Zito, M. Imran, M. Campolucci, Y. P. Ivanov, F. Locardi, I. Infante, G. Divitini and S. Brovelli, Cesium manganese bromide nanocrystal sensitizers for broadband Vis-to-NIR downshifting, *ACS Energy Lett.*, 2022, **7**(5), 1850–1858.

27 P. Sahu and S. P. Mukherjee, Rapid and efficient microwave-assisted synthesis of Mn-doped cesium bromide to phase engineered cesium manganese bromide nanocrystals with color-tunable RGB emission, *J. Mater. Chem. C*, 2025, **13**(19), 9465–9473.

28 J. Cai, X. Zhang, Y. Chen, W. Lai, Y. Ye, S. Xu, Q. Yan, T. Guo, J. Luo and E. Chen, Neuron-inspired  $\text{CsPbBr}_3/\text{PDMS}$  nanospheres for multi-dimensional sensing and interactive displays, *Light: Sci. Appl.*, 2025, **14**(1), 55.

29 J. Cai, W. Lai, Y. Chen, Y. Ye, S. Xu, T. Guo and E. Chen, Ultrawide-Range Wearable Temperature Sensor Utilizing Reversible Luminescence of  $\text{CsPbBr}_3/\text{PS}$  Composites, *Nano Energy*, 2025, 111152.

30 I. López-Fernández, D. Valli, C. Y. Wang, S. Samanta, T. Okamoto, Y. T. Huang, K. Sun, Y. Liu, V. S. Chirvony and A. Patra, Lead-free halide perovskite materials and optoelectronic devices: progress and prospective, *Adv. Funct. Mater.*, 2024, **34**(6), 2307896.

31 H. J. Seifert and E. Dau, Über die Systeme Alkalimetallbromid/Mangan (II)-bromid, *Z. Anorg. Allg. Chem.*, 1972, **391**(3), 302–312.

32 G. Jauncey, The scattering of X-rays and Bragg's law, *Proc. Natl. Acad. Sci. U. S. A.*, 1924, **10**(2), 57–60.

33 H. P. Klug and L. E. Alexander, *X-ray diffraction procedures: for polycrystalline and amorphous materials*, 1974.

34 H. Liang, W. Yang, J. Xia, H. Gu, X. Meng, G. Yang, Y. Fu, B. Wang, H. Cai and Y. Chen, Strain effects on flexible perovskite solar cells, *Adv. Sci.*, 2023, **10**(35), 2304733.

35 M. Wang, Z. Ni, X. Xiao, Y. Zhou and J. Huang, Strain engineering in metal halide perovskite materials and devices: Influence on stability and optoelectronic properties, *Chem. Phys. Rev.*, 2021, **2**(3), 031302.

36 X. Huang, X. Tang, X. Wen, S. Singh, Y. C. Lu and F. Yang, Blue-emitting CsI thin films, *J. Lumin.*, 2025, **280**, 121126.

37 S. Mazumdar, Y. Zhao and X. Zhang, Stability of perovskite solar cells: Degradation mechanisms and remedies, *Front. Electron.*, 2021, **2**, 712785.

38 B. Yang, D. Bogachuk, J. Suo, L. Wagner, H. Kim, J. Lim, A. Hinsch, G. Boschloo, M. K. Nazeeruddin and A. Hagfeldt, Strain effects on halide perovskite solar cells, *Chem. Soc. Rev.*, 2022, **51**(17), 7509–7530.

39 S. Singh, X. Wen and F. Yang, Effect of NaCl on the luminescent behavior of CsI thin films, *RSC Adv.*, 2025, **15**(44), 36993–37005.

40 I. Poli Improving the stability of halide perovskites for photovoltaic applications and solar fuel generation. University of Bath, 2019.

41 S. Macpherson, T. A. Doherty, A. J. Winchester, S. Kosar, D. N. Johnstone, Y.-H. Chiang, K. Galkowski, M. Anaya, K. Frohma and A. N. Iqbal, Local nanoscale phase impurities are degradation sites in halide perovskites, *Nature*, 2022, **607**(7918), 294–300.

42 H. Jin, E. Debroye, M. Keshavarz, I. G. Scheblykin, M. B. Roeffaers, J. Hofkens and J. A. Steele, It's a trap! On the nature of localised states and charge trapping in lead halide perovskites, *Mater. Horiz.*, 2020, **7**(2), 397–410.

43 M. Othman, Q. Jeangros, D. A. Jacobs, M. H. Futscher, S. Zeiske, A. Armin, A. Jaffrès, A. G. Kuba, D. Chernyshov and S. Jenatsch, Alleviating nanostructural phase impurities enhances the optoelectronic properties, device performance and stability of cesium-formamidinium metal-halide perovskites, *Energy Environ. Sci.*, 2024, **17**(11), 3832–3847.

44 Q. Kong, B. Yang, J. Chen, R. Zhang, S. Liu, D. Zheng, H. Zhang, Q. Liu, Y. Wang and K. Han, Phase engineering of cesium manganese bromides nanocrystals with color-tunable emission, *Angew. Chem., Int. Ed.*, 2021, **60**(36), 19653–19659.

45 D. Liang, H. Xiao, W. Cai, S. Lu, S. Zhao, Z. Zang and L. Xie, Mn<sup>2+</sup>-based luminescent metal halides: syntheses, properties, and applications, *Adv. Opt. Mater.*, 2023, **11**(15), 2202997.

46 J. Lin, Q. Zhang, L. Wang, X. Liu, W. Yan, T. Wu, X. Bu and P. Feng, Atomically precise doping of monomanganese ion into coreless supertetrahedral chalcogenide nanocluster inducing unusual red shift in Mn<sup>2+</sup> emission, *J. Am. Chem. Soc.*, 2014, **136**(12), 4769–4779.

47 J. Orive, J. L. Mesa, R. Balda, J. N. Fernandez, J. S. Rodriguez Fernandez, T. Rojo and M. A. I. Arriortua, Enhancement of the luminescent properties of a new red-emitting phosphor, Mn<sub>2</sub>(HPO<sub>3</sub>)<sub>2</sub>, by Zn substitution, *Inorg. Chem.*, 2011, **50**(24), 12463–12476.

48 S. Park, T. Rhodin and L. Rathbun, Halide formation and etching of Cu thin films with Cl<sub>2</sub> and Br<sub>2</sub>, *J. Vac. Sci. Technol., A*, 1986, **4**(2), 168–172.

49 R. Krumpolec, T. Homola, D. C. Cameron, J. Humlíček, O. Caha, K. Kuldová, R. Zazpe, J. Příkryl and J. M. Macak, Structural and optical properties of luminescent copper (I) chloride thin films deposited by sequentially pulsed chemical vapour deposition, *Coatings*, 2018, **8**(10), 369.

50 Q. Kong, X. Xu, Z. Wang, J. Chen and Y. Feng, Multi-Stimuli-Responsive photoluminescence of cesium manganese bromide by temperature and solvent-induced structural phase transitions, *Chem. Eng. J.*, 2024, **485**, 149741.

51 M. Zeng, L. Wei, J. Hu, X. Zeng, G. Li, X. Zhang, Y. Hu, H. Gu and Y. Li, Achieving high transparency and stable luminescence in CsMnBr<sub>3</sub> nanocrystals embedded glass, *J. Eur. Ceram. Soc.*, 2025, **45**(4), 117029.

52 H. Zhang and J. A. Rogers, Recent advances in flexible inorganic light emitting diodes: from materials design to integrated optoelectronic platforms, *Adv. Opt. Mater.*, 2019, **7**(2), 1800936.

53 B. Xu, J. Zhou, C. Zhang, Y. Chang and Z. Deng, Research Progress on Quantum Dot-Embedded Polymer Films and Plates for LCD Backlight Display, *Polymers*, 2025, **17**(2), 233.

54 G. J. Lee, J.-G. Lee, Y. Kim, T. Park, Y. W. Ko and J.-H. Ko, The effect of the reflective property of a reflection film on the performance of backlight units with quantum-dot films for LCD applications, *J. Inf. Disp.*, 2021, **22**(2), 55–61.

55 Z. Luo, D. Xu and S.-T. Wu, Emerging quantum-dots-enhanced LCDs, *J. Disp. Technol.*, 2014, **10**(7), 526–539.

56 S. Hu, X. Yan, Y. Zhang, B. Yang, H. Li and C. Sheng, Light-induced photoluminescence quenching and degradation in quasi 2D perovskites film of (C<sub>6</sub>H<sub>5</sub>C<sub>2</sub>H<sub>4</sub>NH<sub>3</sub>)<sub>2</sub>(CH<sub>3</sub>NH<sub>3</sub>)<sub>2</sub>[Pb<sub>3</sub>I<sub>10</sub>], *Appl. Sci.*, 2021, **11**(6), 2683.

57 N. A. Manshor, Q. Wali, K. K. Wong, S. K. Muzakir, A. Fakharuddin, L. Schmidt-Mende and R. Jose, Humidity versus photo-stability of metal halide perovskite films in a polymer matrix, *Phys. Chem. Chem. Phys.*, 2016, **18**(31), 21629–21639.

58 Z. Song, A. Abate, S. C. Watthage, G. K. Liyanage, A. B. Phillips, U. Steiner, M. Graetzel and M. J. Heben, Perovskite solar cell stability in humid air: partially reversible phase transitions in the PbI<sub>2</sub>-CH<sub>3</sub>NH<sub>3</sub>I-H<sub>2</sub>O system, *Adv. Energy Mater.*, 2016, **6**(19), 1600846.

59 H.-C. Chen, A. Shabir, C. M. Tan, P. Singh and J.-H. Lin, Degradation dynamics of quantum dots in white LED applications, *Sci. Rep.*, 2021, **11**(1), 24153.

60 H. Moon, C. Lee, W. Lee, J. Kim and H. Chae, Stability of quantum dots, quantum dot films, and quantum dot light-emitting diodes for display applications, *Adv. Mater.*, 2019, **31**(34), 1804294.

61 S. Huang, Z. Li, B. Wang, N. Zhu, C. Zhang, L. Kong, Q. Zhang, A. Shan and L. Li, Morphology evolution and degradation of CsPbBr<sub>3</sub> nanocrystals under blue light-emitting diode illumination, *ACS Appl. Mater. Interfaces*, 2017, **9**(8), 7249–7258.

62 C. Balarew, D. Rabadjieva, S. Tepavitcharova, C. Christov and O. Angelova, Thermodynamic study of the aqueous rubidium and manganese bromide system, *J. Solution Chem.*, 1999, **28**(7), 949–958.

63 Q.-C. Yang, D.-F. Qiu, Y.-L. Dang, Z.-P. Qiao and Z.-W. Xu, Phase equilibrium systems of  $\text{CsX} + \text{MnX}_2 + \text{H}_2\text{O}$  ( $\text{X} = \text{Cl}, \text{Br}$ ) at 298.15 K and standard molar enthalpy of formation of  $\text{CsMnX}_3 \cdot 2\text{H}_2\text{O}$  and  $\text{Cs}_2\text{MnX}_4 \cdot 2\text{H}_2\text{O}$ , *J. Chem. Thermodyn.*, 2021, **161**, 106541.

64 W. M. Haynes, *CRC handbook of chemistry and physics*, CRC press, 2016.

65 H. Konieczna, D. Lundberg and I. Persson, Solvation and coordination chemistry of manganese (II) in some solvents. A transfer thermodynamic, complex formation, EXAFS spectroscopic and crystallographic study, *Polyhedron*, 2021, **195**, 114961.

66 Y. Liu, L. Zhang, X. Long, P. Jiang, C. Geng and S. Xu, Ultra-stable  $\text{CsPbBr}_3$  nanocrystals with lead-carboxylate/ $\text{SiO}_2$  encapsulation for LED applications, *J. Mater. Chem. C*, 2021, **9**(37), 12581–12589.

67 J. Park, K. Y. Jang, S. H. Lee, D.-H. Kim, S.-H. Cho and T.-W. Lee, Stable orthorhombic  $\text{CsPbBr}_3$  light emitters: encapsulation-assisted *in situ* synthesis, *Chem. Mater.*, 2023, **35**(16), 6266–6273.

68 F. Boussoufi, M. Pousthomis, A. Kuntzmann, M. D'amico, G. Patriarche and B. Dubertret, Spray-drying polymer encapsulation of  $\text{CsPbBr}_3$  perovskite nanocrystals with enhanced photostability for LED downconverters, *ACS Appl. Nano Mater.*, 2021, **4**(7), 7502–7512.

69 A. Ghosh, L. Gerenser, C. Jarman and J. Fornalik, Thin-film encapsulation of organic light-emitting devices, *Appl. Phys. Lett.*, 2005, **86**(22), 223503.

70 Q. Lu, Z. Yang, X. Meng, Y. Yue, M. A. Ahmad, W. Zhang, S. Zhang, Y. Zhang, Z. Liu and W. Chen, A review on encapsulation technology from organic light emitting diodes to organic and perovskite solar cells, *Adv. Funct. Mater.*, 2021, **31**(23), 2100151.

71 M. A. A. Kazemi, N. Folastre, P. Raval, M. Sliwa, J. M. V. Nsanzimana, S. Golonu, A. Demortiere, J. Rousset, O. Lafon and L. Delevoye, Moisture-Induced Non-Equilibrium Phase Segregation in Triple Cation Mixed Halide Perovskite Monitored by In Situ Characterization Techniques and Solid-State NMR, *Energy Environ. Mater.*, 2023, **6**(2), e12335.

72 C. X. Zhang, T. Shen, D. Guo, L. M. Tang, K. Yang and H. X. Deng, Reviewing and understanding the stability mechanism of halide perovskite solar cells, *InfoMat*, 2020, **2**(6), 1034–1056.

73 J. Li, R. Xia, W. Qi, X. Zhou, J. Cheng, Y. Chen, G. Hou, Y. Ding, Y. Li and Y. Zhao, Encapsulation of perovskite solar cells for enhanced stability: Structures, materials and characterization, *J. Power Sources*, 2021, **485**, 229313.

74 B. McKenna, J. R. Troughton, T. M. Watson and R. C. Evans, Enhancing the stability of organolead halide perovskite films through polymer encapsulation, *RSC Adv.*, 2017, **7**(52), 32942–32951.

75 Q.-F. Li, J.-T. Wang and Z. Wang, Improving the stability of perovskite nanocrystals via  $\text{SiO}_2$  coating and their applications, *RSC Adv.*, 2024, **14**(2), 1417–1430.

76 Y. Yang, H. Chen, C. Liu, J. Xu, C. Huang, C. D. Malliakas, H. Wan, A. S. Bati, Z. Wang and R. P. Reynolds, Amidination of ligands for chemical and field-effect passivation stabilizes perovskite solar cells, *Science*, 2024, **386**(6724), 898–902.

77 E. V. Péan, S. Dimitrov, C. S. De Castro and M. L. Davies, Interpreting time-resolved photoluminescence of perovskite materials, *Phys. Chem. Chem. Phys.*, 2020, **22**(48), 28345–28358.

78 Y. Sun, Y. Wang, H. Zhu, N. Jin, A. Mohammad, N. Biyikli, O. Chen, K. Chen and J. Zhao, Excitation wavelength-dependent photoluminescence decay of single quantum dots near plasmonic gold nanoparticles, *J. Chem. Phys.*, 2022, **156**(15), 154701.

79 S. Wei, J. Hu, C. Bi, K. Ren, X. Wang, N. H. de Leeuw, Y. Lu, M. Sui and W. Wang, Strongly-Confining  $\text{CsPbBr}_3$  Perovskite Quantum Dots with Ultralow Trap Density and Narrow Size Distribution for Efficient Pure-Blue Light-Emitting Diodes, *Small*, 2024, **20**(36), 2400885.

80 L.-Y. Wang, L.-L. Deng, X. Wang, T. Wang, H.-R. Liu, S.-M. Dai, Z. Xing, S.-Y. Xie, R.-B. Huang and L.-S. Zheng, Di-isopropyl ether assisted crystallization of organic-inorganic perovskites for efficient and reproducible perovskite solar cells, *Nanoscale*, 2017, **9**(45), 17893–17901.

81 F. Staub, H. Hempel, J.-C. Hebig, J. Mock, U. W. Paetzold, U. Rau, T. Unold and T. Kirchartz, Beyond bulk lifetimes: insights into lead halide perovskite films from time-resolved photoluminescence, *Phys. Rev. Appl.*, 2016, **6**(4), 044017.

82 S. Bera, A. Saha, S. Mondal, A. Biswas, S. Mallick, R. Chatterjee and S. Roy, Review of defect engineering in perovskites for photovoltaic application, *Mater. Adv.*, 2022, **3**(13), 5234–5247.

83 X. Guan, Y. Li, Y. Meng, K. Wang, K. Lin, Y. Luo, J. Wang, Z. Duan, H. Liu and L. Yang, Targeted elimination of tetravalent-Sn-induced defects for enhanced efficiency and stability in lead-free NIR-II perovskite LEDs, *Nat. Commun.*, 2024, **15**(1), 9913.

84 T. Kirchartz, T. Markwart, U. Rau and D. A. Egger, Impact of small phonon energies on the charge-carrier lifetimes in metal-halide perovskites, *J. Phys. Chem. Lett.*, 2018, **9**(5), 939–946.

85 X. Tang, Y. Zhang, N. L. Kothalawala, X. Wen, D. Y. Kim and F. Yang,  $\text{MAPbBr}_3$  nanocrystals from aqueous solution for poly (methyl methacrylate)- $\text{MAPbBr}_3$  nanocrystal films with compression-resistant photoluminescence, *Nanotechnology*, 2022, **33**(23), 235605.

86 N. Phung, A. Mattoni, J. A. Smith, D. Skroblin, H. Köbler, L. Choubrac, J. Breternitz, J. Li, T. Unold and S. Schorr, Photoprotection in metal halide perovskites by ionic defect formation, *Joule*, 2022, **6**(9), 2152–2174.

87 J. Shi, M. Wang, Z. Da, C. Zhang, J. Wang, Y. Ding, Y. Xu and N. V. Gaponenko, Studies on the optical stability of



CsPbBr<sub>3</sub> with different dimensions (0D, 1D, 2D, 3D) under thermal environments, *Nanoscale*, 2023, **15**(26), 11190–11198.

88 S. Kahmann, O. Nazarenko, S. Shao, O. Hordiichuk, M. L. Kepenekian, J. Even, M. V. Kovalenko, G. R. Blake and M. A. Loi, Negative thermal quenching in FASnI<sub>3</sub> perovskite single crystals and thin films, *ACS Energy Lett.*, 2020, **5**(8), 2512–2519.

89 Q. Zhang, M. He, Q. Wan, W. Zheng, M. Liu, C. Zhang, X. Liao, W. Zhan, L. Kong and X. Guo, Suppressing thermal quenching of lead halide perovskite nanocrystals by constructing a wide-bandgap surface layer for achieving thermally stable white light-emitting diodes, *Chem. Sci.*, 2022, **13**(13), 3719–3727.

90 M. Anni, A. Creti, M. L. De Giorgi and M. Lomascolo, Local morphology effects on the photoluminescence properties of thin CsPbBr<sub>3</sub> nanocrystal films, *Nanomaterials*, 2021, **11**(6), 1470.

91 G. Xiang, Y. Zhou, W. Peng, J. Zhang, Y. Liu, J. Zhang, Z. Yue, X. Zhang, C. Song and B. Ding, Vacuum-deposited perovskite CsPbBr<sub>3</sub> thin-films for temperature-stable Si based pure-green all-inorganic light-emitting diodes, *Ceram. Int.*, 2023, **49**(13), 21624–21633.

92 A. Xie, T. H. Nguyen, C. Hettiarachchi, M. E. Witkowski, W. Drozdowski, M. D. Birowosuto, H. Wang and C. Dang, Thermal quenching and dose studies of X-ray luminescence in single crystals of halide perovskites, *J. Phys. Chem. C*, 2018, **122**(28), 16265–16273.

93 Y. Tang, L. Gomez, M. Van Der Laan, D. Timmerman, V. Sebastian, C.-C. Huang, T. Gregorkiewicz and P. Schall, Room temperature synthesis and characterization of novel lead-free double perovskite nanocrystals with a stable and broadband emission, *J. Mater. Chem. C*, 2021, **9**(1), 158–163.

94 H. S. Bawazir; S. M. Qaid; H. M. Ghaithan; K. K. AlHarbi; A. F. Bin Ajaj and A. S. Aldwayyan, Phase state influence on photoluminescence of MAPb<sub>x</sub>(Br<sub>1-x</sub>)<sub>3</sub> perovskites towards optimized photonics applications, *Photonics*, MDPI, 2022, vol. 10, p. 21.

95 Y. Xu, J. Li, F. Zhao, Y. Gao, R. Chen and T. He, Optical Properties of a CsMnBr<sub>3</sub> Single Crystal, *ACS Omega*, 2022, **7**(33), 29415–29419.

96 S. Ghimire, M. F. Khatun, B. M. Sachith, T. Okamoto, J. Sobhanan, C. Subrahmanyam and V. Biju, Highly Luminous and Stable Halide Perovskite Nanocrystals by Interfacial Defect Passivation and Amphiphilic Ligand Capping, *ACS Appl. Mater. Interfaces*, 2023, **15**(34), 41081–41091.

97 Q. Jing, M. Zhang, X. Huang, X. Ren, P. Wang and Z. Lu, Surface passivation of mixed-halide perovskite CsPb<sub>x</sub>(Br<sub>1-x</sub>)<sub>3</sub> nanocrystals by selective etching for improved stability, *Nanoscale*, 2017, **9**(22), 7391–7396.

98 J. Wiley, Introduction to solid state physics, New York, 1986, 185.

99 G. Horowitz, Organic field-effect transistors, *Adv. Mater.*, 1998, **10**(5), 365–377.

100 N. K. Tailor, C. A. Aranda, M. Saliba and S. Satapathi, Negative photoconductivity: bizarre physics in semiconductors, *ACS Mater. Lett.*, 2022, **4**(11), 2298–2320.

101 N. K. Tailor, P. Maity and S. Satapathi, Observation of Negative Photoconductivity in Lead-Free Cs<sub>3</sub>Bi<sub>2</sub>Br<sub>9</sub>Perovskite Single Crystal, *ACS Photonics*, 2021, **8**(8), 2473–2480.

102 N. K. Tailor, P. Maity, M. I. Saidaminov, N. Pradhan and S. Satapathi, Dark self-healing-mediated negative photoconductivity of a lead-free Cs<sub>3</sub>Bi<sub>2</sub>Cl<sub>9</sub> perovskite single crystal, *J. Phys. Chem. Lett.*, 2021, **12**(9), 2286–2292.

103 S. X. Li, Y. S. Xu, C. L. Li, Q. Guo, G. Wang, H. Xia, H. H. Fang, L. Shen and H. B. Sun, Perovskite single-crystal microwire-array photodetectors with performance stability beyond 1 year, *Adv. Mater.*, 2020, **32**(28), 2001998.

104 B. Sreelakshmi and R. Thamankar, Investigation of the transient photo-response and switching window of an Al/indigo/Al device: unveiling negative photoconductivity and the photo-enhanced memory window, *Mater. Adv.*, 2024, **5**(14), 5912–5921.

105 M. Wang, S. Wang, R. Chen, M. Zhu, Y. Liu, H. Ding, J. Ren, T. Xuan and H. Li, Highly Efficient and Stable CsPbBr<sub>3</sub>-Alginic Acid Composites for White Light-Emitting Diodes, *Coatings*, 2023, **13**(6), 1062.

106 W. Yue, Y. Liu, C. Heyu, L. Chunyang, L. Weizhen, X. Haiyang, Z. Cen, W. Zhongqiang and L. Yichun, White LED based on CsPbBr<sub>3</sub> nanocrystal phosphors via a facile two-step solution synthesis route, *Mater. Res. Bull.*, 2018, **104**, 48–52.

107 D. Tsvetkov, M. Mazurin, I. Ivanov, D. Malyshkin, V. Sereda and A. Zuev, Crucial role of water in the mechanosynthesis of CsPbI<sub>3</sub> and other ABX<sub>3</sub> halides, *Chem. - Eur. J.*, 2020, **26**(55), 12549–12552.

108 S. Xiao, K. Zhang, S. Zheng and S. Yang, Good or evil: what is the role of water in crystallization of organometal halide perovskites?, *Nanoscale Horiz.*, 2020, **5**(8), 1147–1154.

109 X. Shen, K. Kang, Z. Yu, W. H. Jeong, H. Choi, S. H. Park, S. D. Stranks, H. J. Snaith, R. H. Friend and B. R. Lee, Passivation strategies for mitigating defect challenges in halide perovskite light-emitting diodes, *Joule*, 2023, **7**(2), 272–308.

110 L. Gupta, S. Rath, S. Abbi and F. Jain, Temperature dependence of the fundamental band gap parameters in cadmium-rich Zn<sub>x</sub>Cd<sub>1-x</sub>Se using photoluminescence spectroscopy, *Pramana*, 2003, **61**, 729–737.

111 A. Merdasa, M. Bag, Y. Tian, E. Kallman, A. Dobrovolsky and I. G. Scheblykin, Super-resolution luminescence microspectroscopy reveals the mechanism of photo-induced degradation in CH<sub>3</sub>NH<sub>3</sub>PbI<sub>3</sub> perovskite nanocrystals, *J. Phys. Chem. C*, 2016, **120**(19), 10711–10719.

112 S. Meloni, G. Palermo, N. Ashari-Astani, M. Grätzel and U. Rothlisberger, Valence and conduction band tuning in halide perovskites for solar cell applications, *J. Mater. Chem. A*, 2016, **4**(41), 15997–16002.

113 L. Zhang, W. Geng, C.-J. Tong, X. Chen, T. Cao and M. Chen, Strain induced electronic structure variation in methyl-ammonium lead iodide perovskite, *Sci. Rep.*, 2018, **8**(1), 7760.

114 J. Li, X. Yuan, P. Jing, J. Li, M. Wei, J. Hua, J. Zhao and L. Tian, Temperature-dependent photoluminescence of

inorganic perovskite nanocrystal films, *RSC Adv.*, 2016, **6**(82), 78311–78316.

115 E. De Lyle The magnetic anisotropies of manganese-bromide and ferrous-chloride. The University of Chicago, 1964.

116 S. Wu, L. Yuan, G. Chen, C. Peng and Y. Jin, All-inorganic Mn  $2+$ -doped metal halide perovskite crystals for the late-time detection of X-ray afterglow imaging, *Nanoscale*, 2023, **15**(33), 13628–13634.

117 J. Tang, W. Tian, C. Zhao, Q. Sun, C. Zhang, H. Cheng, Y. Shi and S. Jin, Imaging the moisture-induced degradation process of 2D organolead halide perovskites, *ACS Omega*, 2022, **7**(12), 10365–10371.

118 J.-S. Park, J. Calbo, Y.-K. Jung, L. D. Whalley and A. Walsh, Accumulation of deep traps at grain boundaries in halide perovskites, *ACS Energy Lett.*, 2019, **4**(6), 1321–1327.

119 M. A. Haque, J. L. Li, A. L. Abdelhady, M. I. Saidaminov, D. Baran, O. M. Bakr, S. H. Wei and T. Wu, Transition from positive to negative photoconductance in doped hybrid perovskite semiconductors, *Adv. Opt. Mater.*, 2019, **7**(22), 1900865.

120 H. T. Yi, P. Irkhin, P. P. Joshi, Y. N. Gartstein, X. Zhu and V. Podzorov, Experimental demonstration of correlated flux scaling in photoconductivity and photoluminescence of lead-halide perovskites, *Phys. Rev. Appl.*, 2018, **10**(5), 054016.

121 K. M. Tenny and M. Keenaghan Ohms Law. 2017.

122 T. Yata, Y. Miyamoto and K. Ohmi, Emissive Liquid-Crystal Display Panels Consisting of Red-Green-Blue Patterned Phosphor Layers and Near-Ultraviolet Light-Emitting-Diode Backlight, *Jpn. J. Appl. Phys.*, 2012, **51**(2R), 022202.

123 Y.-L. Tong, Y.-W. Zhang, K. Ma, R. Cheng, F. Wang and S. Chen, One-step synthesis of FA-directing FAPbBr<sub>3</sub> perovskite nanocrystals toward high-performance display, *ACS Appl. Mater. Interfaces*, 2018, **10**(37), 31603–31609.

124 Y. Zu, J. Xi, L. Li, J. Dai, S. Wang, F. Yun, B. Jiao, H. Dong, X. Hou and Z. Wu, High-brightness and color-tunable FAPbBr<sub>3</sub> perovskite nanocrystals 2.0 enable ultrapure green luminescence for achieving recommendation 2020 displays, *ACS Appl. Mater. Interfaces*, 2019, **12**(2), 2835–2841.

125 Y. Lu, Y. Xu, S. Chen, J. Lin, J. Zhu, S. Wang, Y. Zheng, F. Huang and D. Chen, Ultra-narrowband emitting and highly stable CsPbX<sub>3</sub>@ glass@ PDMS (X<sub>3</sub> = Br<sub>3</sub>, Br<sub>1.5</sub>I<sub>1.5</sub>) monolithic composite film for backlit displays, *J. Lumin.*, 2022, **248**, 118952.

126 H. Ye, L. Huang, X. Liu, M. Yang, W. Chen, Y. Chen, W. Xiang, S. Pan and X. Liang, Opportunities and challenges in CsPbX<sub>3</sub>@ Glasses@ Film with High Quality for LCD by Process Optimization towards commercialization, *Ceram. Int.*, 2023, **49**(6), 9010–9016.

127 J. Lin, Y. Lu, X. Li, F. Huang, C. Yang, M. Liu, N. Jiang and D. Chen, Perovskite quantum dots glasses based backlit displays, *ACS Energy Lett.*, 2021, **6**(2), 519–528.

128 J. Lin, Z. Zhou, J. Lai, W. Ye, T. Pang, X. Li, L. Zeng, L. Lei, D. Yu and D. Chen, CsPbX<sub>3</sub>@ Glass (X = Cl, Br, I) Nanocomposites with 1 Whole-Family High Absorption Efficiency above 75% for Backlit Display, *Laser Photon. Rev.*, 2025, **19**(4), 2401649.

129 S. Chen, J. Lin, S. Zheng, Y. Zheng and D. Chen, Efficient and stable perovskite white light-emitting diodes for backlit display, *Adv. Funct. Mater.*, 2023, **33**(18), 2213442.

130 C. X. Guo, J. H. Chen, Z. L. He, J. H. Wei and D. B. Kuang, In Situ Growth of MAPbBr<sub>3</sub> Quantum Dots in Crosslinked PMMA for Wide-Gamut Display Backlights, *Small*, 2025, **21**(42), e09037.

131 F. Zhang, J. Song, B. Han, T. Fang, J. Li and H. Zeng, High-Efficiency Pure-Color Inorganic Halide Perovskite Emitters for Ultrahigh-Definition Displays: Progress for Backlighting Displays and Electrically Driven Devices, *Small Methods*, 2018, **2**(10), 1700382.

132 H. C. Wang, S. Y. Lin, A. C. Tang, B. P. Singh, H. C. Tong, C. Y. Chen, Y. C. Lee, T. L. Tsai and R. S. Liu, Mesoporous silica particles integrated with all-inorganic CsPbBr<sub>3</sub> perovskite quantum-dot nanocomposites (MP-PQDs) with high stability and wide color gamut used for backlight display, *Angew. Chem., Int. Ed.*, 2016, **55**(28), 7924–7929.

133 C. Sun, Y. Zhang, C. Ruan, C. Yin, X. Wang, Y. Wang and W. W. Yu, Efficient and stable white LEDs with silica-coated inorganic perovskite quantum dots, *Adv. Mater.*, 2016, **28**(45), 10088–10094.

134 X. Zhang, H.-C. Wang, A.-C. Tang, S.-Y. Lin, H.-C. Tong, C.-Y. Chen, Y.-C. Lee, T.-L. Tsai and R.-S. Liu, Robust and stable narrow-band green emitter: an option for advanced wide-color-gamut backlight display, *Chem. Mater.*, 2016, **28**(23), 8493–8497.

135 K. Ma, X.-Y. Du, Y.-W. Zhang and S. Chen, In situ fabrication of halide perovskite nanocrystals embedded in polymer composites via microfluidic spinning microreactors, *J. Mater. Chem. C*, 2017, **5**(36), 9398–9404.

136 J. Y. Sun, F. T. Rabouw, X. F. Yang, X. Y. Huang, X. P. Jing, S. Ye and Q. Y. Zhang, Facile two-step synthesis of all-inorganic perovskite CsPbX<sub>3</sub> (X = Cl, Br, and I) zeolite-Y composite phosphors for potential backlight display application, *Adv. Funct. Mater.*, 2017, **27**(45), 1704371.

